CCFE
CULHAM CENTRE FOR FUSION ENERGY

UK Atomic Energy Authority

UKAEA-CCFE-PR(19)24

B C G Reman, R O Dendy, T Akiyama, S C Chapman,
J W S Cook, H Igami, S Inagaki, K Saito, G S Yun

Interpreting observations of ion cyclotron emission from Large Helical Device plasmas with beam-injected ion populations

Interpreting observations of ion cyclotron emission from Large Helical Device plasmas with beam-injected ion populations

B C G Reman, R O Dendy, T Akiyama, S C Chapman, J W S Cook,
H Igami, S Inagaki, K Saito, G S Yun

This is a preprint of a paper submitted for publication in
Nuclear Fusion

Interpreting observations of ion cyclotron emission from Large Helical Device plasmas with beam-injected ion populations

B. C. G. Reman[1], R. O. Dendy[2,1], T. Akiyama[3], S. C. Chapman[1], J. W. S. Cook[2], H. Igami[3], S. Inagaki[4], K. Saito[3], and G. S. Yun[5]

[1]Centre for Fusion, Space and Astrophysics, Department of Physics, Warwick University, Coventry CV4 7AL, UK

[2]CCFE, Culham Science Centre, Abingdon, Oxfordshire OX14 3DB, UK

[3]National Institute for Fusion Science, Toki, Gifu 509-5292, Japan

[4]Research Institute for Applied Mechanics, Kyushu University,

Kasuga 816-8580, Japan

[5]Department of Physics, Pohang University of Science and Technology, Pohang 37673, Korea

Abstract

Ion cyclotron emission (ICE) is detected from all large toroidal magnetically confined fusion (MCF) plasmas. It is a form of spontaneous suprathermal radiation, whose spectral peak frequencies correspond to sequential cyclotron harmonics of energetic ion species, evaluated at the emission location. We first present an account of the worldwide experimental ICE database, highlighting the phenomenological importance of the value of the ratio of energetic ion velocity $v_{Energetic}$ to the local Alfvén speed V_A. We then focus on ICE measurements from heliotron-stellarator hydrogen plasmas, heated by energetic proton neutral beam injection (NBI) in the Large Helical Device, for which $v_{Energetic}/V_A$ takes values both larger (super-Alfvénic) and smaller (sub-Alfvénic) than unity. The collective relaxation of the NBI proton population, together with the thermal plasma, is studied using a particle-in-cell (PIC) code. This evolves the Maxwell-Lorentz system of equations for hundreds of millions of kinetic gyro-orbit-resolved ions and fluid electrons, self-consistently with the electric and

magnetic fields. For LHD-relevant parameter sets, the spatiotemporal Fourier transforms of the fields yield, in the nonlinear saturated regime, good computational proxies for the observed ICE spectra in both the super-Alfvénic and sub-Alfvénic regimes for NBI protons. At early times in the PIC treatment, the computed growth rates correspond to analytical linear growth rates of the magnetoacoustic cyclotron instability (MCI), which was previously identified to underly ICE from tokamak plasmas. The spatially localised PIC treatment does not include toroidal effects or geometry. Its success in simulating ICE spectra from both tokamak and, here, heliotron-stellarator plasmas suggests that the plasma parameters and ion energetic distribution at the emission location suffice to determine the ICE phenomenology. The capability to span the super-Alfvénic and sub-Alfvénic energetic ion regimes is a generic challenge in interpreting MCF plasma physics, and it is encouraging that this first principles computational treatment of ICE has now achieved this.

1 Introduction

Suprathermal ion cyclotron emission [1, 2] (ICE) is detected from all large toroidal magnetic confinement fusion (MCF) plasmas including the tokamaks TFR [3], PDX [4], JET [5], TFTR [6], JT-60U [7], ASDEX-U [8],

KSTAR [9], DIII-D [10] and the stellarators LHD [11, 12] and W7-AS [13]. ICE is notable as the first collective radiative instability driven by confined fusion-born ions that was observed in deuterium-tritium (D-T) plasmas in JET and TFTR [14, 15, 16, 17]. The frequency spectrum of ICE typically exhibits narrow peaks at values which can be identified with sequential local cyclotron harmonics of a distinct energetic ion population in a spatially localised emitting region. The numerical value of the inferred ion cyclotron frequency $\Omega_c = Z_i eB/m_i$, where Z_i is the ion charge and m_i its mass, then determines the local value of the magnetic field strength in the emitting region, and hence its radial location. Typically, but not invariably, this is at the outer mid-plane edge of the toroidal plasma; ICE from the core plasma has been reported recently from DIII-D [18] and from ASDEX-Upgrade [19], , and earlier from JT-60U [7]. This development suggests great potential for the exploitation of ICE as a diagnostic for energetic particles in ITER [20]. Measurements of ion cyclotron emission (ICE) spectra have been obtained from heliotron-stellarator plasmas in the Large Helical Device (LHD), both with an ICRH antenna during NBI heated plasmas [11] and by magnetic probes [12] during toroidal Alfvén eigenmodes (TAE's) [21, 22, 23, 24]. Related numerical studies can be found in [24]. In combination with other advanced diagnostics, notably for MHD activity, these ICE measurements from LHD, which we analyse here, can yield fresh insights into the physics

of energetic ions in magnetically confined fusion (MCF) plasmas, and into the interaction between these ions and MHD activity. Exploitation of these advanced, high resolution ICE measurements requires a correspondingly advanced modelling capability for its most likely emission mechanism, which is the magnetoacoustic cyclotron instability (MCI) [25]. Here we analyse ICE spectra which we attribute to a neutral beam injected (NBI) proton population at energies $\approx$ 40keV in the outer midplane edge regions of hydrogen plasmas in LHD [11, 12], where the local electron temperature T_e $\approx$20eV to 150eV, number density $n_e \approx 10^{19}\mathrm{m}^{-3}$ and magnetic field strength $B \approx 0.5$T. These spectra were measured with an ICRF heating antenna in receiver mode. Importantly, these spectra span plasma regimes where the ratio of the velocity of the energetic ions V_{NBI} to the local Alfvén speed V_A in the ICE-emitting region of the LHD edge plasma takes values that can be either smaller or larger than unity. The transition between super-Alfvénic and sub-Alfvénic energetic ion phenomenology is of fundamental interest in MCF plasma physics. Here, in particular, we examine LHD plasmas 79126 and 79003 where $V_{NBI}/V_A = 0.872$ and 1.125, respectively, in the ICE-emitting region. We follow the full velocity-space trajectories, including gyromotion, of tens to hundreds of millions of fully kinetic energetic and thermal ions, together with all three vector components of the evolving electric and magnetic fields, with a massless neutralising electron fluid,

using a fully nonlinear 1D3V PIC-hybrid particle-in-cell code [26]. The kinetic ions, fluid electrons, and fields are coupled self-consistently through the Lorentz force and Maxwell's equations in Darwin's approximation [27]. In this hybrid scheme [26], the Debye length does not need to be resolved. It therefore requires less computational resource than the full PIC scheme implemented in EPOCH [28], which retains electron kinetics, and is also used for contemporary theoretical studies of ICE [29, 30, 31, 32, 33]. We follow these simulations through the linear phase of an instability that we show is the MCI, and then deeply into its nonlinear saturated phase. The Fourier transforms of the excited fields yield frequency spectra that match the observed ICE spectra from the LHD plasmas. These simulation results for heliotron-stellarator plasmas complement and confirm earlier interpretation of ICE driven by sub-Alfvénic NBI ions in TFTR tokamak plasmas [34, 15]. ICE was also previously measured in the W7-AS stellarator [13] by broadband loop antenna during hydrogen NBI.

The rapid recent growth in the research literature on ICE measurements and their interpretation means that a mini-review is becoming due. Section 1 of this paper attempts to supply this, in order to place in context the ICE results from LHD, and our first principles computational modelling of them, which are reported in Section 2 onwards. A central theme of Section 1 is that ICE phenomenology reflects the plasma parameters and magnetic field

strength in the emitting region, together with the velocity distribution of the driving energetic ion population. Important aspects of these two key features come together in the dimensionless parameter $v_{Energetic}/V_A$, which is the ratio of energetic ion velocity $v_{Energetic}$ to the local Alfvén speed V_A. We highlight the role of this parameter in ICE phenomenology and modelling in Section 1 as it arises.

1.1 Early measurements of ion cyclotron emission

1.1.1 In JET

ICE was first reported from the TFR tokamak [3]. Measurements followed from JET, where ICE was detected with an ICRF heating antenna in receiver mode from Ohmic and NBI-heated plasmas [5, 35, 36, 37, 1]. Strongly suprathermal spectral peaks at cyclotron harmonics and half harmonics of protons in deuterium plasmas were described in [5]. Large radial drift excursions of fusion-born ions were identified as the underlying driver for JET ICE, because these give rise to a velocity-space inversion at the emission location [36]; collective radiation through the MCI then follows [38, 39, 40, 41, 16, 17]. Inverted sawtooth oscillations in the ICE signals from sawtoothing JET Ohmic plasmas were also reported early [16]. The ICE intensity was proportional to the measured deuterium fusion reactivity R_{DD} over three orders of magnitude. From observations of time delays relative to the soft X-ray

(SXR) sawtooth crash, see Fig. 3 of [35], the ICE sawtoothing was interpreted in terms of an enhancement of fusion activity in the edge plasma following the arrival of a sawtooth heat pulse.

With the introduction of tritium into JET in 1991 [42], ICE was detected at successive cyclotron harmonics of α particles. The intensity of this ICE extended the linear correlation with the measured neutron flux [36] to over six decades of signal intensity across all classes of JET plasma.

No clear correlation of ICE with fishbone bursts was obtained from JET [36]. During H-mode discharges, two types of ELMs, identified as small and large, were reported. The antenna-plasma coupling resistance R_c is always observed to increase during ELM events, so that the correlation of ICE with small ELMs was attributed to a change in R_c rather than to intrinsic changes in the ICE power. In contrast, ICE disappeared for about 20ms at the time of large ELM events which were believed to expel fast ions from the plasma edge, thereby extinguishing the ICE source. In summary, from early measurements on JET: the frequency matching to local magnetic field strength that follows from the observation of ICE spectral peaks at successive cyclotron harmonics; the disappearance of ICE with large ELMs which penetrate 10-30cm into the edge plasma; and correlation of the time-evolution of the ICE signal with edge α particle density, all point to emission that originates from the outer midplane edge (Fig. 10 [36]) and is driven by

fusion-born ions.

1.1.2 In TFTR

Demonstrations of fusion α-particle generation soon followed in TFTR deuterium (D) and tritium (T) plasmas including DT-supershots [43], during which ICE was also reported [6]. Dedicated radio-frequency probes were installed close to the top and the bottom of the vacuum vessel, situated in a vertical plane intersecting the magnetic axis, at poloidal angles of $\pm 90°$ with respect to the outer midplane. Each array of seven probes could distinguish between electrostatic and electromagnetic signals. ICE was observed with spectral peaks corresponding to the outer midplane edge cyclotron harmonics of fusion products (^{3}He in DD supershots, and both ^{4}He and ^{3}He in T and in DT supershots) and of NBI-injected D and T. During the first 50 to 200 ms following the NBI trigger, cyclotron harmonics of the fusion products dominated the measured ICE spectrum, but then died out. They were replaced by ICE spectral peaks at multiple cyclotron harmonics of the injected D and T, until the NBI injectors were turned off. This time evolution contrasts with ICE from JET, where ICE due to fusion-born ions persisted for the entire duration of the discharge. In subsequent TFTR experiments, He was puffed [44], forcing the plasmas to transit from typical supershots to pure L-modes. This changed the plasma density and hence the local

value of the ratio v_α/V_A ($\lesssim 1$), where v_α is the α-particle birth velocity and V_A is the local Alfvén speed in the ICE-emitting region at the plasma edge. In TFTR supershots, the α-particle fusion products are sub-Alfvénic in the edge plasma. As discussed in section 1.4.1, this may account for the transient nature of the ICE associated with fusion product ions, which is restricted to the early stage of the discharge. A plasma shifting from supershot to L-mode leads to early α-driven ICE generation lasting for $\approx$ 200ms which then soon extinguishes, typical of the supershot phase, see Fig. 7 of [6]. The α-driven ICE is subsequently regenerated at the time of the He puff which increases the edge density and thereby v_α/V_A, such that 3.5MeV α-particles become super-Alfvénic. The α-driven ICE signal persists during that phase until the NBI is turned off, see Fig. 8 of [6]. In the pure L-mode TFTR plasmas, this α-driven ICE prevailed for the entire duration of the discharge, until the beams were switched off, see Fig. 9 of [6]. Across multiple TFTR DT plasmas, the peak intensity of ICE whose fundamental frequency corresponded to the α-particle cyclotron frequency Ω_α at the edge, correlated with the measured neutron flux. This reinforces the identification of fusion-born ions as the driving population. The spectrum of NBI Triton-ICE from TFTR displays relatively lower intensity at harmonic numbers 3 and 6, which may be due to cyclotron resonant absorption by the bulk deuterium, see Fig. 2 of [34]. The foregoing account of observed

ICE phenomenology from TFTR DT plasmas provides some clear instances of the motivation for the present study. It suggests that investigation of the ways in which the ratio $v_{NBI}/V_A \lesssim 1$ affects the physics of ICE in LHD is of generic interest.

1.1.3 In JT-60

In early ICE measurements from the JT-60 tokamak, an electrostatic signal was observed at the second cyclotron harmonic of protons during perpendicular H NBI into hydrogen plasmas [45]. Correlation with charge-exchange analysers placed the origin of this ICE signal at the edge of the torus, where a fast ion tail was generated. The ICE was observed only if the beam protons had energies no higher than 40 keV, and the intensity of the ICE appeared to be proportional to tail temperature. It was considered that resonant damping of ICE waves was further energising fast ions, such that the tail did not undergo significant thermalization. The intensity of the ICE signal was greater at higher plasma density. This may reflect the increase in the ratio of proton injection speed to local Alfvén speed, see Fig. 2 of Ref. [46], although the instability considered was electrostatic and not observed at energies above 40keV. ICE from JT-60 plasmas was observed in limiter magnetic geometry. In this configuration, NBI protons can undergo large banana orbit excursions which, it was noted, could give rise to velocity-

space anisotropy at the outer midplane edge and perhaps drive the Harris instability [46], which is predominantly electrostatic.

1.1.4 In JT-60U

Subsequent to Ref. [46], JT-60 was upgraded with a divertor to enable H-mode operation, and become JT-60 U, from which ICE measurements were reported in [7]. These include the detection of ICE from fusion-born tritons in the core of JT-60U deuterium plasmas; no corresponding phenomenon was reported from JET or TFTR. The parallel and perpendicular electric fields were measured by means of three RF probes installed below an ICRF antenna. The first three harmonics of tritons were observed at 21MHz corresponding to a major radius of 3.1-3.2m. The emission from the core (due to T) was positively correlated with ELMs and peaked at ELM onset, as can be seen from the D_α signal in Fig 16 of Ref. [7]. Conversely, ELMs anti-correlated with ICE signals that originated from the edge. The third D harmonic (82MHz corresponding to a major radius of 3.87m) was at its minimal amplitude at the maximum of the ELM. ICE from the outer edge at proton cyclotron harmonics was also identified. The underlying instability was identified with the MCI due to the relatively much smaller parallel component of the electric field that was observed. This implies excitation of predominantly electromagnetic waves, specifically the fast Alfvén wave

which is generated by the MCI. As in JET and in TFTR [47, 44], no ICE occurred in conjunction with toroidal Alfvén eigenmodes (TAEs).

1.2 Recent measurements of ion cyclotron emission

1.2.1 In JET

Simultanenous use of different antennas enabled the observation of ICE from JET plasmas during ICRH scenarios [37] which were designed to simulate the behaviour of fusion product ions by using the ICRH-heated minority proton population. The ICE originates from the outer midplane edge of the plasma, like fusion product-driven ICE (FP-ICE) on JET. A distinctive feature of this minority ion-driven ICE (mICE) is the observed time delay between the ICRH antenna turn-on and the initiation of ICE. This is accounted for by the time needed for initially thermal ICRH-resonant protons to be accelerated and form a tail of fast ions in velocity space that is capable of destabilising waves on the fast-Alfvén ion-cyclotron branch. The threshold for detecting mICE is primarily governed by the radio frequency power P_{rf} delivered to the plasma and by the stored energy in the fast ions W_{fast}. In JET hydrogen plasmas, ICE has been detected with the Sub-Harmonic Arc Detection (SHAD) system from minority energetic ^{3}He ions [48, 49] subjected to ICRH. The frequency range of the SHAD system is limited such that only the fundamental cyclotron frequency can be detected. The ICE

spectra featured sub-structures spaced by a few kHz which are thought to correspond to CAEs [50]. The SHAD system detected ICE soon after the radio frequency power P_{rf} ramp-up for most plasmas, suggesting that the drive is supplied by the minority ^{3}He. ICE was also detected with modulated ICRH power when it reached its flat-top, shortly after the step-down of the NBI pulse, and following the disappearance of a magnetic fluctuation identified as a 3/2 neoclassical tearing mode. The intensity of this mode correlated with fast ion losses when the ICRH was reaching its peak. It is thought that classical fast ion confinement was recovered when the tearing-mode died out. This can account for the subsequent ICE emission in the edge as a result of large orbit excursions of fast ^{3}He ions. This is supported by energy profile calculations with the PION code [49] and related computed fast ion trajectories. Full 1D3V PIC and hybrid-PIC simulations were run [49] using the local plasma and fast ion parameters, including both parallel and perpendicular velocities of the fast ions at the last closed flux surface. These were obtained using magnetic moment conservation for 2MeV ^{3}He ions, born moving perpendicular to the magnetic field at the resonance location. These velocities then specify the initial ring-beam and drifting-Maxwellian distribution functions that are used to characterise the ^{3}He ion population at the start of the PIC and PIC-hybrid simulations. The resulting simulated power spectra display peaks at successive ^{3}He cyclotron harmonics, including the

fundamental as detected by the SHAD system.

1.2.2 In JT-60U

ICE driven by NBI and fusion-born energetic ions was identified in JT-60U [45, 51], and the spatial structure of the wave components in the poloidal and toroidal directions was studied [52]. Positive ion based neutral beams (P-NBI) were used for perpendicular and tangential beam injection, along with negative-ion based neutral beams (N-NBI) in the tangential direction. Two sets of ICRF antennae were used as pickup loops, separated by 1.67m in the toroidal direction. Each antenna consists of an array of four loops set up in two rows and two columns: the straps (vertical arrays) are separated by 44 cm, see Fig. 1 of [52]. This enables measurement of toroidal mode numbers by computing phase differences obtained from adjacent toroidal straps. The poloidal straps of the antenna are used to distinguish between electrostatic and electromagnetic perturbations [53]. ICE during perpendicular P-NBI of D ions was detected at multiple cyclotron harmonics of Ω_D, at a value implying a magnetic field strength corresponding to a location just inside the outermost flux surface at the outer midplane. Rich structure was present in the dynamical evolution of the ICE: for example, odd harmonics were excited at the beginning of the NBI, whereas even modes were strongly driven later. ICE was also reported in hydrogen JT-60U plasmas heated

by NBI protons. [52]. FP-ICE, distinguished also by its sharp spectral peaks, was only observed during tangential NBI in deuterium plasmas. Its cyclotron frequencies correspond to a locus slightly beyond the outermost magnetic surface. Two intense peaks were detected at the onset of the 80keV tangential P-NBI of deuterons followed later by perpendicular P-NBI. These were identified as the first two cyclotron harmonics of fusion-born ^{3}He ions in the plasma midplane edge. Their intensity weakened or disappeared with increasing density, and the ^{3}He fundamental was especially sensitive [53]. As the perpendicular P-NBI power increased from 4 to 8MW, it was accompanied by the generation of broad D cyclotron harmonic peaks. This phenomenology is very similar to the transient observations of FP-ICE in TFTR [6], discussed in section 1.1.2. A single peak identified as FP T ICE arose later, after the start of the tangential N-NBI (450keV, 3MW), at higher density and neutron emission rate compared to the conditions under which the FP ^{3}He ICE fundamental and its harmonics were excited. The FP-T peak frequency was slightly below the value of Ω_T at the outermost magnetic surface. The intensity scaled linearly with the measured neutron flux, unlike FP ^{3}He ICE. It was concluded that some ICE excitations could exhibit structure with very low m. ICE due to FPs displayed toroidal mode structure, whereas ICE due D-NBI did not. The magnitude of $k_\parallel$ was higher for T than for ^{3}He, estimated to be respectively 10m^{-1} and 3m^{-1} at their

fundamental cyclotron frequency. The finite toroidal wavenumber of FP-ICE was exploited to distinguish the fundamental of FP H ions from the second harmonic of D-NBI ions in this ICE data [51], owing to the zero toroidal wavenumber of NBI-driven ICE in JT-60U. The signal is sensitive to the density and was observed during weak magnetic shear operation [54, 51], which could be a necessary condition underlying FP H ICE. Splitting of spectral peaks reported in JET FP-ICE [55, 56], was also observed in JT-60U for the case of FP ^{3}He ICE propagating in both toroidal directions.

1.3 Contemporary measurements

1.3.1 In ASDEX-Upgrade

ICE measurements from AUG, reported in [8, 57], were measured with cross dipole antennas and a voltage probe inside an ICRH antenna. Four types of ICE were identified: FP, beam and ICRH-driven ICE, all occurring in the edge; and core ICE. In NBI-heated discharges with power above 5MW, ICE bursts at the fundamental of ^{3}He were followed by diffuse D NBI ICE, similar to JT-60U and TFTR. When the power was above 10MW, a spectral peak just below the second D harmonic was identified to be ICE driven by FP H ions because the intensity of the signal strongly correlated with the neutron rate, reminiscent of FP H-driven ICE in JT-60 U, see Section 1.2.2. Subsequent measurements have been taken [58] using as diagnostics a system

of pairs of B-dot probes [19] (inductors) installed on both the low- and high-field sides (LFS and HFS) of the torus. A hydogen plasma in H-mode exhibited classical ICE originating from the edge, driven by H-NBI at 52keV and 72keV, with frequency 30MHz. The signal was modulated by ELM crashes.

Importantly, ICE emitted from the core is also reported from D plasmas in ASDEX-Upgrade, heated with 60keV D-NBI in both H-mode and L-mode regimes [8, 57]. The fundamental of H or second D harmonic is observed, along with the second H harmonic (or fourth D harmonic) in plasmas at lower field magnetic field. This core ICE takes two forms. It appears as a transient at the beginning of the NBI phase within the first 100ms during which an inversion or anisotropy in velocity space could exist [59]. The ICE signal is sensitive to the magnetic field value on axis, which evolves with the pressure profile [8]. In addition, core ICE is observed during steady-state operation and dies out after as long as one second, when the NBI changes orientation from tangential to more perpendicular. Splitting is observed within the ICE spectral peaks, with separations of 100kHz to 200kHz, and there is additional fine structure with separation in the low tens of kHz. These structures are also seen in ICE associated with ICRH minority H heating (mICE) in ASDEX [8]. Fast ion full-orbit tracking codes indicate that pitch angles corresponding to $v_{\|}/v$ above 0.45 for co-current beam operations and

below -0.72 for counter-current beams lead to confined FP H trajectories. These ions are super-Alfvénic in the core of ASDEX-Upgrade, and thus more likely to drive ICE by the magnetoacoustic cyclotron instability (MCI) [38] than to the D-NBI ions which are sub-Alfvénic at that location.

1.3.2 In DIII-D

Measurements of ion cyclotron emission originating from the plasma core were recently reported from the DIII-D tokamak and correlate with beam ion losses [60]. The ICE signals were obtained using an antenna strap in deuterium plasmas, heated by eight deuterium NBI beams. These are oriented either mainly parallel or mainly perpendicular with respect to the toroidal magnetic field. The injection direction can be co-current (6 beams; parallel) or counter-current (2 beams; anti-parallel). The measured magnetic fluctuations at the second harmonic of deuterium ($\sim$ 30MHz) were substantial during tangential injection, particularly in the co-current direction. A signal probably corresponding to the fourth cyclotron harmonic of deuterium at the outer midplane edge was also reported. ICE during perpendicular NBI injection was extremely weak in comparison, perhaps surprisingly because prompt losses of fast ions are greater in this configuration. These differences were investigated by focusing on the spatial distribution of the beam ions and on the loss strike structures along the wall. During quiescent

H-mode plasmas characterized by reversed current directions, three beams were oriented parallel to the counter-current direction, and three perpendicular. Prompt loss and ionization profiles were computed with a Monte Carlo code that takes the scrape-off layer into account. The profiles between the different beams were similar (density of ionization events and wall strikes) but the toroidal location strikes were quite different, indicating the ICE measurements dependence on the beam geometries. ICE was also detected from Helium plasmas heated by a Helium neutral beam in DIII-D [60]. The frequency of the dominant spectral peak is identified with the fourth cyclotron harmonic of He in the plasma core, and the time evolution of its intensity broadly followed the edge density while the power of the beams remain constant. The results were consistent with the beam ion losses and wall strikes as in the corresponding deuterium case. The degeneracy of the Helium cyclotron frequency with that of D can create difficulties in distinguishing the roles of these two species in driving ICE signals. However, as described in Section 1.2.2, toroidal mode number measurements distinguish between ICE driven by fusion-born protons and NBI deuterons at the same frequency $\Omega_H = 2\Omega_D$. A similar approach may in future be applicable to He-driven ICE.

Subsequently, in 2017, two antenna loops in the outer carbon wall DIII-D were restored along with an antenna probe for low and high bandpass mea-

surements [18], completing the initial system of two antennae straps. These two systems are separated toroidally by 50°. The acquisition system can resolve signal frequencies up to 200MHz, digitized at 200MSamples/s for about 5s, thus generating 32GB of data per plasma. Signals were identified across three physically distinct frequency regimes. First, there is classical ICE whose spectral peak frequencies f correspond to harmonics of f_{ci}, the ion cyclotron frequency, with $5 \leq f \leq 100$MHz. Lower frequency magnetic fluctuations are sometimes observed, and are attributed to compressional Alfvén eigenmodes (CAE's) with $f < f_{ci}$ (2-10MHz). Emission probably corresponding to whistler waves with $f \gg f_{ci}$ (100-200MHz), destabilized by MeV runaway electrons, is identified [61] with the same diagnostic. The ICE originates both from the plasma centre during L-mode plasmas at $R = 1.8$m, as inferred from the EFIT equilibrium reconstruction code [18], and from the outboard edge. A rich phenomenology is emerging from the DIII-D ICE measurements [62], including the detection of ICE from the plasma core both at early times during NBI plasmas and during L-mode phases. The more common edge ICE typically arises driven during multi-beam D NBI heated H-mode deuterium plasmas. It exhibits spectral peaks which are broader than those associated with ICE from the plasma core. Weak ICE signals were also detected during Ohmic and ECH plasmas but are not well understood. A thorough study [62] of the effect of beam characteristics on

the ICE signal has been carried out, including the influence of the triangularity [63] on the ICE location: positive triangularity is associated with edge ICE (H-mode) whereas negative triangularity is associated with core ICE, which is weaker. Plasmas heated with co-current off-axis NBI do not generate much central ICE, which is stronger with on-axis beams, particularly perpendicular beams. In addition, the central ICE fundamental cyclotron frequency is modified between tangential and perpendicular co-beam operation. It is observed that tangential beams oriented in the counter-current direction generate more core ICE power than counter-perpendicular beams; this may be due to possible voltage difference. Counter-current beams excite more ICE, located more centrally, than co-current beams. The central ICE magnitude appears to increase with voltage, a possible consequence of increased v_{beam}/V_A but is not affected by NBI heating power. The magnitude of prompt losses amounts to 1.6% for co-tangential beams associated with the lowest ICE power, while it was 2.9% for co-perpendicular beams and was as high as 27.2% in counter-tangential beams [62].

The dependence of ICE signals on beam characteristics was also investigated during H-mode plasmas in DIII-D [62]. The spectral peaks are observed to broaden due to superposition when co-current NBI power increases. The addition of counter-current NBI power further increases ICE intensity and the number of cyclotron spectral peaks harmonic [62]. In this case, prompt

losses vary between 0.4% and 0.6% in the case of co-beams, and reach 23% for counter-beams.

Off-axis fishbones detected in DIII-D have been characterized as an $n = 1$ mode driven by neutral beam ions [10], and ICE was among the diagnostics in this study. The mode is responsible for the loss of fast ions, which peaks spatially close to the location of the maximum mode amplitude. This is demonstrated in Fig. 11 of Ref. [10] which shows phase space of energetic ions at different major radii in the midplane. It displays the associated passing, trapped and lost fast ion trajectories, along with the locations of the precessional resonance and the central beam deposition. The trajectories are constructed by assuming conservation of magnetic moment μ, of energy W and of canonical angular momentum P_ϕ in a collisionless regime. The beam, precessional resonance and lost ion trajectories locations in phase space can all intersect, such that a small toroidal angular momentum change generated by the off-axis fishbone can lead to loss. The instability takes place in the edge, at major radius $R \approx 2.25m$. As many as seven diagnostics studied the instability, including ICE, which was measured by means of a high-bandwith toroidal coil [10]. The signal was filtered by a low-pass and a high-pass filter. These respectively resolve ICE spectral peaks at the fundamental deuterium cyclotron frequency, and at the second and third D harmonics. The ICE signal correlated with the beacon-like Mirnov bursts,

particularly the high-pass ICE signals, and was phase-shifted relative to the beacon mode, a general feature observed in several diagnostics. This reliable correlation suggests that initially the fast ions are expelled, then they drive the MCI in the plasma edge, resulting in ICE signals which provide a good measure of the timing and magnitude of the fast ion losses [10].

1.3.3 In KSTAR

A qualitative step forward in the measurement and understanding of ICE has followed from the recent application of new antenna diagnostics [9] with very high sampling rates $> 1\text{GSas}^{-1}$ and bandwidth > 1 GHz to plasmas in the conventional aspect ratio KSTAR tokamak [9, 20]. In KSTAR [9, 64] deuterium H-mode plasmas heated by deuterium NBI, downward chirping ICE was driven by a small, hitherto unanticipated, sub-population of confined fusion-born protons passing through the edge plasma, whose density rapidly declines during an ELM crash. The distribution of energy across successive fixed cyclotron harmonic frequencies in the ICE signal changes rapidly ("chirping"), on microsecond timescales, probably associated with ELM filament bursts. This striking phenomenology represents the final stage of ICE signal time evolution associated with an ELM. Previous stages include a pre-crash broadband and continued radiation at around 200MHz, perhaps corresponding to the lower hybrid frequency in the KSTAR plasma

edge, followed by ICE intensification at cyclotron-harmonic spectral lines of D or H, as well as wide-band continuum RF excitations at the crash onset. ECE imaging at that time shows the burst of a non-modal filamentary structure which expels heat, then followed by rapid RF chirping. Multiple simulations of the MCI [32] for KSTAR edge plasma conditions with the relevant fusion-born proton population, spanning density values from $n_{pedestal}$ to a small fraction thereof, generated different spectra whose properties match those of the chirping ICE. The mapping from density in the simulations to time in the chirping ICE observations enables sub-microsecond time resolution of the evolving local edge density, probably reflecting ELM filament dynamics. The extremely high resolution time series from KSTAR have unveiled transient "ghost" ICE features [9], above the lower hybrid frequency, between 500MHz and 900MHz, slightly offset by 1μs from their ICE counterparts below 500MHz. These features evolve on microsecond time scales and have been demonstrated to result from nonlinear wave-wave coupling [33] between the dominant RF waves in the ICE spectral feature below 500MHz. Importantly, these dynamical higher frequency ICE spectral structures also chirp downwards, and PIC simulations show that this can be accounted for by the pedestal density collapse.

1.4 Introduction to ICE theory and interpretation

1.4.1 Analytical theory of the magnetoacoustic cyclotron instability

The magnetoacoustic cyclotron instability (MCI) [41, 34, 65, 30, 26] is the most likely emission mechanism to account for ICE generation. The theory of the MCI was developed analytically between the 1970s and 1990s, and using large PIC numerical simulation from 2010 onwards [29, 31, 66]. At the plasma wave-particle resonant level of description, the MCI essentially involves the resonance of a fast Alfvén wave supported by the background plasma with negative-energy ion cyclotron harmonic waves sustained by minority fast ions whose non-Maxwellian velocity distribution incorporates a population inversion. The theory was originally developed by Belikov and Kolesnichenko [25] for purely perpendicular propagating waves satisfying $\omega \gg \Omega_i$, the background ion cyclotron frequency, including a ring beam distribution for fast ions. The theory was revisited and extended by Dendy et al. [38] to lower frequencies for perpendicular propagation, and MCI growth rates were further obtained for energetic ion distributions in velocity space that have the form of both a spherical and an extended-spherical shell [39], in addition to monoenergetic ring beams [25, 67]. The interest in the ring beam-type distribution arose from the subset of fast ions thought to be responsible for generating ICE from DT plasmas in JET and, subsequently,

TFTR. These ions, born in a very narrow range of pitch angles, undergo large drift orbit excursions from the core whose trajectories intersect the outer midplane edge. This leads to a local population inversion in velocity space, in the form of a thin cone shape which is limited by: the maximum energy of the α particles; their narrow range of pitch angles; and, at the lower bound, the strong decrease of radial excursion with decreasing energy (Fig 15 of [36]).

The fully kinetic analytical treatment of the MCI [34, 65] included a finite background temperature. This contributes to a stabilisation of the MCI for fast ions having a mono-energetic ring-beam distribution, due to positive energy loading: background ions enter into cyclotron resonance with an initially unstable mode, preventing its further growth. A critical beam density exists, below which the ℓth cyclotron harmonic is stable [25, 38]. The impact of a drifting ring-beam with a finite perpendicular thermal spread was explored in [67] for perpendicular propagation at low β for parameters relevant to space plasmas. The associated growth rates of the MCI can be greatly reduced and can be considered in terms of a continuous band of ring beam speeds or of k-values, see Fig. 3 of Ref. [67], particularly when $ku/\Omega > u/v_r$, where u and v_r are the drift and spread velocites respectively. This is equivalent to stating that the finite spread of a ring could prevent cyclotron harmonic instability for frequencies $\omega > (V_A/v_r)\,\Omega$. In [68], lin-

ear theory at higher β for conditions relevant to the terrestrial bow shock, showed that a moderate thermal spread in the ring suppressed instabilities at cyclotron harmonics, beginning with higher ones for perpendicular propagation. In the oblique propagation case, strong instability was deduced for a mono-energetic ring in a bi-Maxwellian background plasma which can lead to a merging of adjacent harmonics into a continuum. This is reminiscent of Fig 1.a. in [26]. An extended ring was expected to reduce cyclotron harmonics instabilities as well. The Alfvén ion cyclotron instability ($k_{\|} \gg k_{\perp}$) was on the contrary most strongly driven by a extended-ring [68] whose temperatures are equal in the perpendicular and parallel directions.

Ring-beam distributions are also appropriate for representing freshly ionised populations of neutral beam-injected (NBI) ions, and were used in initial studies of the excitation of electrostatic modes [69, 70] to interpret probe measurements of ICE in TFTR plasmas with deuterium and tritium NBI [34]. This instability did not on rely on the fast Alfvén wave, and could be driven by significantly sub-Alfvénic fast ions given a very narrow distribution of speeds parallel to the magnetic field. Computed growth rates for T harmonics degenerate with background D were relatively lower, providing a link with the observed reduced intensity of ICE spectral peaks at the of third and sixth T harmonics in some TFTR experiments, see Fig. 2 of [34]. The instability was shown to involve a sensitive trade-off between the

relative beam ion density $\xi = n_{beam}/n_e$ and their parallel velocity spread v_r, with a large enough v_r eventully halting the instability. This sensitivity could account for the edge location of the NBI-driven ICE, assuming a greater spread of beam ion velocities deeper in the plasma, whereas it was the narrow range of energy and pitch angles of fast ions that were driving ICE at the edge of JET.

ICE from fusion-born alpha-particles was subsequently observed from TFTR DT supershot plasmas [44]. As in JET, the emitting region was the outer midplane edge, populated by confined ions that had undergone large drift orbit excursions from their birth location in the plasma core, see Fig.2 of [44]. These ions had a much larger spread in parallel velocities than in previous instances of ICE, and this led to a reexamination of the MCI [65]. Its underlying theory [71] was further generalized [65] to include finite parallel propagation, incorporating cyclotron damping and electron transit time damping. Electron Landau damping was neglected as the wave electric field was assumed to be polarized perpendicular to the background magnetic field. The Doppler shifts arising from the finite $k_{\|}$ in the resonance condition had the effect of decoupling the MCI drive from bulk ion cyclotron resonant damping, such that instability can take place at extremely low fusion ion densities. This extended theory [71] was applied for parameters matching the form of population inversion in velocity-space expected from fusion-born

alpha-particles in the ICE-emitting region at the outer midplane edge in JET and TFTR (Fig. 16 of [14]). As noted in Section 1.1.2, in contrast to JET, where ICE driven by fusion-born ions tended to persist throughout the duration of the plasma, in typical TFTR NBI-heated discharges, ICE with spectral peaks at successive cyclotron harmonics of fusion-born ions was only observed during the first 100 ms of the plasma, followed by ICE with spectral peaks at NBI ion cyclotron harmonics. The fast ions in TFTR were sub-Alfvénic under the plasma conditions at the location of emission, whereas they were super-Alfvénic in JET. For the MCI, this distinction leads to different growth rates, higher in JET's case, accounting for the different ICE phenomenology as follows. In JET, the maximal radial excursion r_{max} of α particles was slightly smaller than a, the minor radius, while in TFTR supershots $r_{max} > a$. Therefore, the velocity inversion wedge for FP-driven ICE in TFTR was wider than in JET DT plasmas [5, 14], and than that for beam-driven ICE in TFTR. Before the TFTR core alpha-particle distribution broadens, the wedge becomes evenly filled so that a finite thermal spread exists before significant collisions occur. The fusion reactivity increased at the beginning of the supershot while the alpha-particle distribution simultaneously started to broaden, having initially been extremely narrow at the edge due the narrow range of pitch angles for which large orbits arise. Thus, there are at least two critical and competing time scales con-

trolling the edge velocity distribution in terms of anisotropy and narrowness: the fusion ion slowing-down time τ_{slow}, and the neutron rise time τ_N [43]. It was suggested that if $\tau_{slow} < \tau_N$, broadening of the alpha-particle distribution dominates over its replenishment and prevents velocity space inversion [59]. These parameters inferred from measurements were used to feed Sigmar's model for the approximate evolution of the alpha-particle distribution function [72, 65]. The associated spread in velocity space was assumed to apply in the edge, and was used as the spread of a drifting bi-Maxwellian in the analytical calculation of the generalised MCI growth rates [65]. A striking correlation was obtained between the maximum linear growth rates computed this way and the time evolution of the ICE amplitude averaged over six TFTR supershots, see Fig. 6 of [65]. The saturation process was not clearly identified but nonlinear wave-wave interaction was suggested. While linear theory makes no assumption on the initial wave amplitude, it appeared that growth rates were strong enough to amplify its power well above the noise level [14]. The growth rates scaled linearly with the fusion ion density and were relatively sensitive to thermal spread. It was further shown that under the MCI, a sub-Alfvénic fast ion population needs some degree of velocity-space anisotropy to be unstable, while an infinitely thin isotropic shell of super-Alfvénic ions can be unstable, equations 18 and 19 of [14]. This absence was most probably due to the monotonically decreasing

slowing-down alpha-particle distribution in the core plasma [73, 65]. In [40], the possibility of driving ICE through density gradients was considered, for $k_{\|} = 0$, by examining the instability threshold of the drift-cyclotron loss-cone anisotropy (DCLC). This is important since ICE originated in the edge of TFTR plasmas, where a steep gradient exists. For $k_{\|} = 0$ it was concluded that DCLC was not destabilized in TFTR.

ICE measurements obtained in ICRH and NBI heated JET DT plasmas were analysed in [74]. A classical alpha-particle confinement model was applied to obtain an approximate slowing-down distribution of the core alpha particles [72], assuming that they interact with the plasma primarily via Coulomb collisions, and that prompt losses can be neglected. This solution was also used to infer the parameters of an assumed drifting bi-Maxwellian distribution, with equal parallel and perpendicular velocity spreads. This model was adopted for the location of ICE emission at the JET edge, following the observation that the edge distribution was more peaked than the core distribution in velocity space. It was demonstrated [74] that the linear theory of the MCI applied to this specific distribution gave rise to instability. In addition, an unexplained spectral feature was accounted for by ion hybrid waves [75]; the tritium density at the ICE location leads to an ion hybrid frequency which matches the observed frequency. Further generalization in Ref. [76] included the curvature and grad B drifts in the linear analysis which was

applied to JET plasmas, and further applied to TFTR DT plasmas [76], resulting in increased growth rates. A distribution function calculated for the JET edge plasma based on trapped ion banana orbits was considered in Ref. [77] and shown to be unstable against the MCI. Additional work investigated consequences for the MCI of the finite size of the banana orbit [78].

In JT-60 U, FP-^{3}He ICE was attributed to the MCI at oblique propagation [71, 52]. The dispersion relation for Maxwellian D and ^{3}He was solved for the relevant plasma parameters (simulations pertaining to ^{3}He are reviewed in Section 1.4.3). It was demonstrated that Bernstein waves supported by FP ^{3}He could resonate with the Alfvén wave supported by thermal D, at the second harmonic, and that resonance at $\Omega_{^3He}$ was not possible ICE due to FP T was hypothesized to be a consequence of resonance with the slow Alfvén wave which can be unstable to temperature anisotropy. The reason was twofold: first its wavenumber was relatively larger, second the observed frequency was smaller than the T cyclotron frequency Ω_T at the outermost magnetic surface in JT-60 U plasma edge. ^{3}He ions born in the centre could not reach the edge, and this could suggest why ^{3}He-driven ICE was mostly observed to be transient.

1.4.2 Initial computational modelling of ICE

The advent of NBI as a heating scheme drove early interest in the instabilities that could be driven by the resulting fast ion population in the plasma. This motivated an early study [79] of the MCI relevant to NBI heating scenarios in Doublet-3. The distribution of the fast ions was computed using a bounce-averaged Fokker-Planck code for near perpendicular beam injection, for both Doublet-3 and PDX plasma parameters. The initial beam energies were 80-40-27 keV for Doublet-3 and 38-19 keV in the case of PDX. The form of the distribution calculated in the equatorial plane allowed the evaluation of $T_\perp/T_\parallel$, the ratio of perpendicular and parallel temperatures lying in the range 2.3 to 7.7. An approximate dispersion relation for weak damping and growth was derived at arbitrary propagation angle with respect to the background magnetic field in slab geometry [79]. Inversion in velocity space, $\partial F_0^\alpha/\partial v_\perp > 0$, with F_0^α the fast ion distribution function, was indicated to be the primary trigger of the MCI. It was found that it could also be driven with $\partial F_0^\alpha/\partial v_\parallel > 0$ for an anisotropic Maxwellian, provided that the parallel resonance velocity was negative, or that ω is just below the ℓ harmonic. The focus for instability was then placed on anisotropy. The dispersion relation was developed for a Maxwellian background distribution along with an anisotropic Maxwellian-like distribution for the fast ions $\propto v_\perp^{2n} \exp\left(-v_\perp^2/v_{\perp,\alpha}^2 - v_\parallel^2/v_{\parallel,\alpha}^2\right)$ with $v_{\perp,\alpha}$ and $v_{\parallel,\alpha}$, the characterising

perpendicular and parallel velocity spread. A density instability threshold ξ_{crit} of 4% was obtained [79] with an anisotropic Maxwellian for the fast ions characterized by $T_{\perp,\alpha}/T_{\parallel,\alpha} \gg 1 \gg T_0/T_{\parallel,\alpha}$, with T_0 the background temperature. The latter condition arises from the background stabilizing effect. A single Bessel function term was retained near resonance; all other terms in the series composing the dispersion relation were neglected. Expanding the Bessel function to first order, it was concluded that linear growth rate values could be up to a few percent of Ω_α and was decreasing for increasing harmonic number. The study did not retain electron transit-time and Landau damping, which were two orders of magnitude smaller than cyclotron damping. The interaction of the MCI with fast particles trapped in toroidal geometry and having $\partial F_0^\alpha/\partial v_\perp > 0$ was also investigated, assuming a background magnetic field strength of the form $B(\theta) = B_0(1 + \epsilon\cos\theta)$, with the inverse aspect ratio $\epsilon = r/R$ and θ the poloidal angle. This expression was used in the generalised analytical treatment of the MCI by Fülöp and Lisak [76]. A dispersion relation for the case of this inhomogeneous magnetic field was obtained by transforming time integrals into sums over particle orbits expressed by integrals over the angle θ.

1.4.3 First principles numerical simulations of ICE

Direct numerical simulations of ICE scenarios were first reported in 2013 [30]. These used a particle-in-cell (PIC) [80, 81, 82] code [28] (see also Sec. 3) to evolve the full orbit kinetics of millions of thermal ions and electrons, together with the self-consistent electric and magnetic fields, all governed by the Maxwell and Lorentz equations. The distribution of energetic ions in velocity space is typically initialised to reflect physics considerations relevant to the observations of ICE. PIC simulations motivated by ICE measurements from JET show [30, 26] that energetic minority ions relax, under Maxwell-Lorentz dynamics, in ways that replicate the linear MCI at early times and, at later times, produce power spectra capturing measured ICE features. Multiple simulations with different concentrations of energetic ions give rise to a linear scaling of spectral peak intensity that matches the observed linear scaling of ICE intensity with fusion activity [66] in JET. Simulations of the MCI using PIC and PIC-hybrid modelling in their non-linear phase have produced power spectra matching experimental observations [30, 26] and have demonstrated the linear scaling of ICE with fusion activity [66] in JET edge plasma. An ICE-related scenario relevant to α-channelling [83] has been proposed on the basis of PIC simulations [31]. It rests on a process that can arise when a radially inward propagating fast Alfvén wave, unstable against the MCI in the outer edge plasma, thereby extracts energy from a

fast ion population and transfers it to the bulk plasma.

In [84], the velocity distribution of fusion-born ions in JT-60U was evolved with an orbit following code. This required tracing the orbits of NBI deuterons and integrating the associated beam-thermal deuteron-deuteron fusion reactivity over time to obtain a spatial distribution profile for the resulting ^{3}He ions, assumed to be born isotropically in velocity space with energy 0.82MeV. The drift orbits of the ^{3}He ions were then evolved, and shown to give rise to a population inversion in velocity space near the JT-60U plasma edge, as required to excite the MCI and hence drive ICE. In addition, Ref. [84] solves the generalized analytical dispersion relation for a thermal D plasma with a ring-beam ^{3}He distribution (eq.1 of [41]), yielding toroidal wavenumbers $k_{\|} \sim 3\mathrm{m}^{-1}$ and frequencies ω that match experiments. The negative $k_{\|}$ value computed accounts for the observed frequency ω of the ^{3}He ICE spectral peak being slightly lower than the ^{3}He cyclotron frequency $\Omega_{^3He}$ in the plasma edge. This is interpreted by the Doppler-shifted resonance condition for the MCI [1], $\omega - k_{\|}V_d - \ell\Omega_{^3He} = 0$ where V_d is the drift velocity along the local magnetic field and ℓ an integer. The transient behaviour of FP ^{3}He ICE, which disappeared during JT-60U N-NBI, was accounted for in [85] by numerically solving the the full dielectric tensor, in the uniform case, for non-Maxwellian velocity distributions that represent ^{3}He behaviour as obtained from a full-orbit code. Growth rates of the MCI were calculated

for relative densities of ^{3}He FP compared to thermal deuterons as low as 10^{-8} in the edge plasma, capturing FP ^{3}He ICE characteristics.

2 ICE measurements from NBI-heated LHD hydrogen plasmas

Highly resolved ICE signals were measured in LHD hydrogen plasmas using an ICRF antenna in receiver mode [11] during perpendicular neutral beam injection (NBI) of hydrogen ions. The large antenna loop area ($\approx 600\text{cm}^2$) enhances the quality of the data, which was recorded at a maximum sampling rate of 5GSas^{-1} and processed via fast Fourier transform, with a rectangular window of typical duration 100μs. Examples of time profiles of heating with four proton NBI sources, together with ICE spectra, are shown in Figures 1 and 2. These ICE signals are detected shortly after the turn-on of the perpendicular positive-ion based NB injector #4 by an antenna located close to it, at the outer midplane of LHD. The fundamental ICE frequency f_0 is defined by the measured interval between successive spectral peaks, and also typically corresponds to the frequency of the first measured spectral peak. A linear relation was obtained between f_0 and the magnitude of the magnetic field on axis (at a major radius of 3.6m) across several LHD plasmas, confirming the cyclotronic character of the detected signal.

It follows that the location at which this ICE signal is generated in LHD lies along a magnetic field line on which the proton cyclotron frequency f_{cH} corresponds to the measured fundamental ICE frequency f_0, see Figs. 3 and 4 of [11]; this is found to be at both the LHD plasma inner and outer edge in the LHD magnetic configuration (see Fig. 3 [11]). The observation of ICE from high density ($n_e > 5 \times 10^{20}\mathrm{m}^{-3}$) LHD plasmas, into which NBI cannot penetrate as far as the inner edge, further supports the interpretation that ICE originates from the outer region near the NBI #4 injection point. The ICE signal disappeared roughly 0.1ms after the turn-off of the perpendicular NBI (see Fig 5 of [11]). This synchronization suggests that ICE is driven by the fast injected protons. Particle orbit calculations [11] for the relevant LHD plasma and magnetic field show that NBI protons are lost in a few tens of microseconds, consistent with the observed decay time of ICE.

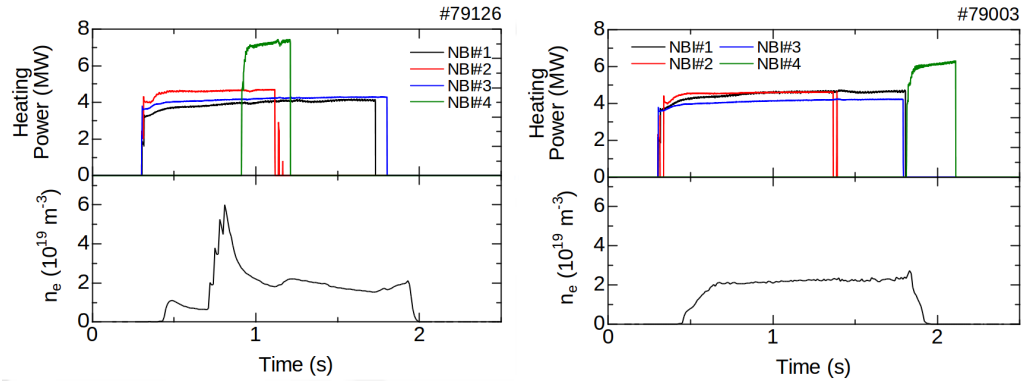

Figure 1: Time histories of NBI evolution (top panels) and line-integrated densities (bottom panels) in sub-Alfvénic LHD plasma 79126 (left) and in super-Alfvénic LHD plasma 79003 (right). In both cases, the ICE is concurrent with perpendicular NBI #4, at t≈1.210s (left) and at t≈1.817s (right).

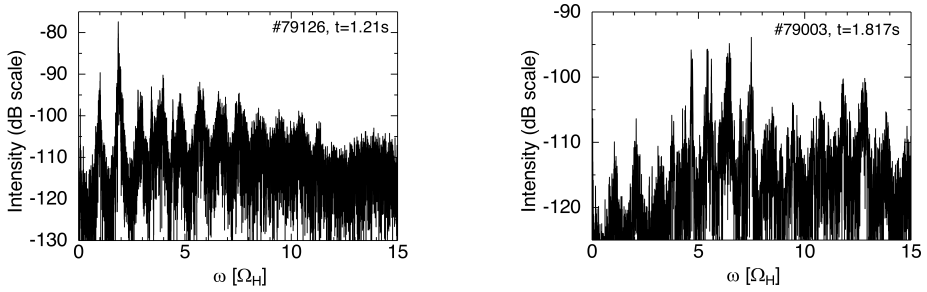

Figure 2: ICE spectra measured on LHD. Left panel: B field power spectrum for perpendicular 40 keV sub-Alfvénic NBI proton from LHD plasma 79126. The radiation originates at $R_{ax} = 4.62$m corresponding to $\Omega_H = 6.75$MHz, which we identify with the observed separation f_0 between successive spectral peaks, see Fig. 3 (left). The local plasma temperature $T_e \approx 150$eV and density $n_e \approx 10^{19}\mathrm{m}^{-3}$. Right panel: B field power spectrum for perpendicular 36.5 keV super-Alfvénic NBI proton from LHD plasma 79003. The radiation originates at $R_{ax} = 4.65$m corresponding to $\Omega_H = 3.67$MHz, the observed separation between successive spectral peaks, see Fig. 3 (right). The local plasma temperature $T_e \approx 25$eV and density $n_e \approx 0.5 \times 10^{19}\mathrm{m}^{-3}$.

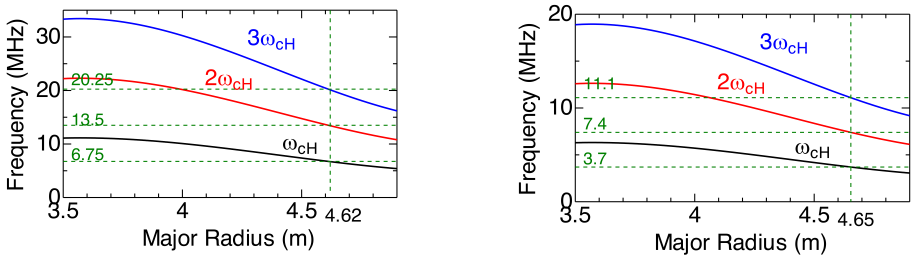

Figure 3: Dependence of the local value of the proton cyclotron harmonic frequencies on major radial position in LHD plasmas 79126 (left) and 79003 (right). The measured spectral peak separations f_0 in Fig. 2 are identified with the proton cyclotron frequencies $\Omega_H = 6.75$MHz and $\Omega_H = 3.67$MHz respectively. The corresponding magnetic fields have magnitude 0.46T and 0.24T. We infer that ICE is emitted at $R_{ax} = 4.62$m (left) for LHD plasma 79126, and at $R_{ax} = 4.65$m (right) for LHD plasma 79003.

3 Experimental information on the NBI proton population in LHD plasmas

In this paper, we will interpret the ICE spectra shown in Figs. 1 and 2, in terms of the collective relaxation of the NBI proton population in the LHD plasma edge. This study requires, as input, a representation of the distribution in velocity-space of the NBI protons. We are fortunate that kinetic modelling [86] has previously been used to obtain the steady-state distribution function of NBI fast ions in stellarators, for both TJ-II and LHD. The LHD case focused on hydrogen plasmas heated by 40keV perpendicular NBI, relevant to our study. The orbit code ISDEP (Integrator of Stochastic Differential Equations for Plasmas) [86] is a Monte Carlo orbit-following code which solves the Fokker-Planck equation in 5D phase space, namely: (x, y, z, v^2, λ). The three spatial coordinates (x, y, z) are the guiding centre position, v^2 is a normalised kinetic energy, and $\lambda = \mathbf{v}\cdot\mathbf{B}/vB$ is a pitch angle. ISDEP includes collisions of fast ions with background ions and electrons, and treats re-entering particles. The initial NBI ion distribution function is calculated with HFREYA [87] which simulates the evolution of fast neutral particles by modelling their propagation, charge exchange and ionization processes. The resulting distribution in Bustos et al. [86]'s work, which is relevant to perpendicular NBI in LHD, presents distinct features. This

includes the pitch angle λ peaking near zero, whose $\sim$ 34keV NB component is close to the 36.5 keV super-Alfvénic initial fast proton population which, as we shall show, drives the ICE. The distribution is localized toroidally and increases with ρ, the dimensionless plasma radius defined in terms of toroidal flux surfaces. This NBI proton population is thus expected to arise close to NBI # 4, and therefore close to the ICRF receiver antenna. We shall thus incorporate this form of minority energetic proton population in our first principles modelling of ICE in LHD.

The top left and bottom left panels of Fig. 4, from Ref. [86], show the time evolution of the average energy and persistence of the fast ions. The persistence P corresponds to the probability that fast ions are still in the plasma at a specific time t following the injection at $t = 0$. There is a prompt loss phase shown by the sudden decrease of P around $t \sim 0.5 \times 10^{-4}$s, which is is very close to the time scale on which ICE decays following the NBI turn-off [11]. The average kinetic energy, shown at the top right of Fig. 4, does not change until later. A second phase inferred from the persistence graph corresponds to the slowing-down time of the fast protons, taking place on millisecond time scales, between $t \sim 10^{-3}$s and $t \sim 10^{-2}$s. For $t > 10^{-2}$s, fast NBI ions undergo loss of confinement. The slowing-down time as a function of plasma radius was also inferred in Bustos et al. [86] from ISDEP calculations, yielding good agreement. Comparison with the decay time of

neutral flux intensities obtained from fast neutral analyzers during LHD radial pulsed NBI experiments (NB-blip) [88, 89] was performed, and some variations owing to the different energy range and time scales were identified. In [89], losses were attributed to pitch-angle scattering. The ion lifetime suggested good confinement properties, particularly in the inward-shifted configuration.

The right panel of Fig. 4 (reproduced from Ref. [86]) shows the velocity distribution function of the fast ions computed with ISDEP [86], sampled at points where they hit the vacuum vessel, at three different times associated with the phases identified on the persistence graph at the bottom right corner of Fig. 4. We infer from these that ICE occurs before significant slowing-down has taken place, on sub millisecond time scales due to prompt losses of NBI ions in LHD. These losses result in a strongly anisotropic distribution of the lost ions in velocity space which, as we shall show in this paper, is capable of driving ICE at the LHD plasma edge. The modelled and measured distribution functions of fast NBI ions in the LHD plasma edge thus provide compelling evidence for this strongly anisotropic character. This guides the choice of a ring-beam distribution to represent the velocity distribution of the NBI protons in our PIC-hybrid simulations (Section 3).

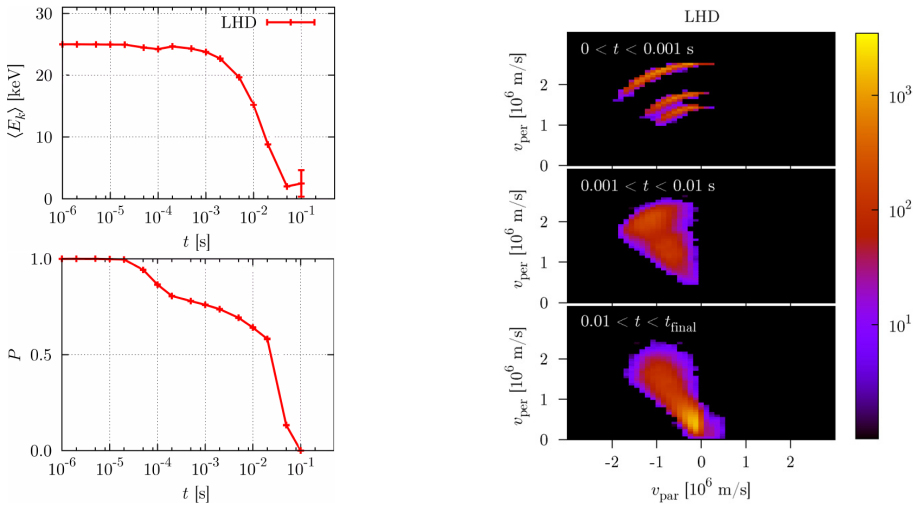

Figure 4: Left panel: Time evolution of the average energy (top) and persistence (bottom) of perpendicular NBI hydrogen in LHD plasmas computed with the code ISDEP [90]. The persistence is defined as the probability that fast ions have remained in the plasma at a given time. Three phases are identified: prompt losses ($t \sim 0.5 \times 10^{-4}$ to 10^{-4}s), slowing-down phase ($t \sim 10^{-4}$ to 10^{-2}) and loss of confinement $t > 10^{-2}$, computed with ISDEP. Panels reprinted with permission from A. Bustos *et. al.* 2011 *Nucl. Fusion* **51** 083040 [86]. Right panel: Velocity space distribution computed with the code ISDEP [90] and representing the escape of perpendicular NBI hydrogen in LHD when they hit the vacuum vessel. The different graphs correspond to different times, early times at the top and later times at the bottom. A wedged-shape, strongly anisotropic distribution is visible, which diffuses in velocity space at later times. Panel reprinted with permission from A. Bustos *et. al.* 2011 *Nucl. Fusion* **51** 083040 doi:10.1088/0029-5515/51/8/083040 [86]. These are motivating our choice of the fast ion distribution function.

4 Direct numerical simulation of LHD ICE using a kinetic PIC-hybrid code

4.1 The PIC-hybrid approach

We use the one spatial dimension and three velocity space dimensions (1D3V) PIC-hybrid code [91, 92] approach implemented in Ref. [26]. This follows full gyro-orbit kinetics for ions in collisionless plasmas, where the energetic and thermal populations are represented by hundreds of thousands to hundreds of millions of macro-particles. These interact with each other, and with the self-consistent electric and magnetic fields, through the Lorentz force and Maxwell's equations. The code incorporates all three vector components of the electric and magnetic fields, and of each particle's velocity, and represents the electrons as a massless neutralising fluid. It self-consistently solves and iterates the Lorentz force equation for each particle together with Maxwell's equations in the Darwin approximation [20, 91]; it is fully non-linear. The code resolves ion gyromotion, which is necessary to simulate phenomena such as ICE where key physical length scales and time scales are of the order of the ion gyro-radius (and ion skin depth) and ion cyclotron frequency. In particular, the code captures the full spatial and gyrophase dynamics of resonant particle-field interactions close to the ion cyclotron

frequency and its harmonics. We assume quasineutrality:

$$\sum_{l=1}^{N} Z_l n_l = n_e \tag{1}$$

with n_e the number density of electrons and n_l, Z_l the number density and electric charge of each ion species l. We also have

$$\nabla \cdot \mathbf{B} = 0 \Rightarrow B_x = 0 \tag{2}$$

where x denotes distance along the 1D slab geometry spatial domain of our code. We solve for $\mathbf{B}$ using Faraday's law

$$\frac{\partial \mathbf{B}}{\partial t} = -\nabla \times \mathbf{E} \tag{3}$$

while Ampère's law in the Darwin approximation [27] combines with the massless electron momentum equation to give the generalized Ohm's law [93],

$$\mathbf{E} = \frac{1}{\mu_0 e n_e} (\nabla \times \mathbf{B}) \times \mathbf{B} - \mathbf{V}_i \times \mathbf{B} - \frac{\nabla p_e}{e n_e} \tag{4}$$

Here the charge-weighted mean ion velocity $\mathbf{V}_i$ is defined by

$$\mathbf{V}_i = \frac{\sum_{l=1}^{N} Z_l n_l \mathbf{u}_l}{\sum_{l=1}^{N} Z_l n_l} \tag{5}$$

where $\mathbf{u}_l$ denotes the bulk ion velocity of species l. We assume an isothermal pressure law, $p_e = n_e k_B T_e$, with T_e the electron temperature. A quiet start [94, 80] is used to launch the majority thermal ions in phase space, so as to reduce the noise in our simulations. The code makes use of periodic boundary conditions. This level of approximation is known to sustain fluid waves such as the fast Alfvén and whistler waves, as well as kinetic waves such as electrostatic Bernstein and ion cyclotron modes.

4.2 Physical and computational parameter sets

The NBI protons are sub (super)-Alfvénic in the emitting region of LHD hydrogen plasmas 79126 (79003), whose measured ICE spectra are shown in Fig. 2 and again in Fig. 8. Their initial energies are 40 keV (36.5 keV), corresponding to a proton perpendicular injection velocity $v_{NBI} = 2.77 \times 10^6 \mathrm{ms}^{-1}$ ($2.64 \times 10^6 \mathrm{ms}^{-1}$). To approximately represent LHD edge plasma conditions in the simulations reported here, the thermal electrons and ions both have a temperature of 0.150 (0.025) keV, the electron density is $10^{19}\mathrm{m}^{-3}$ ($5 \times 10^{18}\mathrm{m}^{-3}$), and the background magnetic field has strength $B_0 = 0.46$ (0.24)T. The local Alfvén speed V_A is therefore 3.17 (2.35) $\times$ $10^6 \mathrm{ms}^{-1}$, hence the NBI protons are sub (super)-Alfvénic with $v_{NBI}/V_A \approx$ 0.870 (1.125). In our simulations, the 40 (36.5) keV NBI proton population is taken to have particle concentration $\xi = 5 \times 10^{-4}$ (7.5×10^{-4}) relative

to the thermal ions. It is represented by an initial ring-beam distribution in velocity space, $f_{NBI}\left(v_{\parallel}, v_{\perp}\right) = \delta(v_{\parallel})\delta\left(v_{\perp} - v_{NBI}\right)$ where the NBI protons are initially uniformly and randomly distributed in gyro-angle. Denoting the spatial component of the 1D3V simulation domain by $\hat{\mathbf{x}}$, the wavevector $\mathbf{k} = k\hat{\mathbf{x}}$; in our simulations, the angle between $\mathbf{B}_0$ and $\mathbf{k}$ is 89.5°. There are 22080 (10560) computational cells and 4000 (500) macroparticles per cell. The cell size is 0.61 (1.06) times the thermal ion Larmor radius $r_L =$ 0.0031 (0.0025)m; for neutral beam ions $r_{L,NBI} = 0.063$ (0.115)m. This implies that the simulations resolve 1.35 (1.12) $\times 10^4$ background proton gyroradii or 670 (240) NBI fast proton gyroradii. The time step is 0.00025 (0.0001) $\times \tau_H$, where $\tau_H = 0.143\mu s$ ($\tau_H = 0.273\mu s$) is the proton gyroperiod in each simulation. Cyclotron motion is thus highly resolved, in space and time, for the energetic ions whose cyclotron resonant collective relaxation underlies the observed ICE signals. The simulations run for 10 to $100\tau_H$; this is determined by the time taken for the instability driven by the NBI ions to saturate, which for a given set of plasma parameters depends on ξ and on propagation angle. Physical and computational parameters for our simulations are summarized in Table 1. When necessary, subcycling for the electric and magnetic fields is used to satisfy the CFL condition for the Alfvén wave [95]. In our simulations, energy is conserved within 0.2%.

Quantity	Plasma 79126	Plasma 79003
Regime	sub-Alfvénic	super-Alfvénic
Simulation duration	$[6, 15] \times \tau_H$	$[12, 25] \times \tau_H$
T_{NBI}	40 keV	36.5keV
v_{NBI}/V_A	0.870	1.125
Length of simulation domain	$670 \times r_{NBI}$ $13500 \times r_L$	$240 \times r_{NBI}$ $11175 \times r_L$
$\cos^{-1}\left(\hat{\mathbf{k}} \cdot \hat{\mathbf{B}}_0\right)$	$89, 5°, 85°$	$89.5°, 85°$
$\xi = n_{NBI}/n_e$	$[0.10, 0.60] \times 10^{-3}$	$[0.10, 1.90] \times 10^{-3}$
Number of grid cells	22080	10560
Number of part. per cell	4000	500
$T_e = T_H$	150eV	25eV
n_e	$1.0 \times 10^{19}\mathrm{m}^{-3}$	$0.5 \times 10^{19}\mathrm{m}^{-3}$
B_0	0.46T	0.24T
Δx	0.0019m	0.0026m
λ_D	2.35×10^{-5}m	1.35×10^{-5}m
λ_e	0.0017m	0.0024m
λ_H	0.0720m	0.1019m
r_L	0.0031m	0.0025m
β	0.19×10^{-4}	5.78×10^{-4}
ω_H/Ω_H	94.46	127.58

Table 1: Summary of the physical and computational parameters used in the PIC-hybrid ICE simulations for LHD plasmas 79126 and 79003.

4.3 Results of PIC-hybrid simulations

Figure 5 plots the time evolution, in our simulations, of the energy density of the electric and magnetic fields, and of the kinetic energy density of the bulk proton and NBI proton populations. The four panels of Fig. 5 are for sub-Alfvénic (left) and super-Alfvénic (right) NBI protons, and for propagation angles θ of $\mathbf{k}$ with respect to $\mathbf{B}_0$ of 89.5° (top) and 85° (bottom). It is evident that the time taken for the NBI fast protons, which are not replenished, to relax, and for the instability which we identify below with the MCI to unfold, saturates on time scales of between $10\tau_H$ to $100\tau_H$. This corresponds to a few microseconds to a few 100 microseconds, and is broadly consistent with the observed decay time of ICE at the NBI turn-off in LHD [11]. The relative NBI proton concentration $\xi = n_{NBI}/n_e$ is chosen small enough to observe the unfolding of the MCI, yet not too small to reach saturation in a tractable computing time and for the ICE power to remain above the noise level. For this reason, the beam density is an order of magnitude higher ($\xi = 0.005$) in the 79126 sub-Alfvénic LHD plasma simulation with propagation angle 85° compared with the other 3 simulations. The energy released at saturation by this 40keV NBI proton population is one order of magnitude higher as a result, as can be observed from the bottom left panel of Fig 5. More generally, the collisionless relaxation of the NBI protons under the MCI is slower at a propagation angle of 85.0° between the wavevector $\mathbf{k}$ and the

background magnetic field $\mathbf{B}_0$ (bottom panels of Fig. 5) than it is at a propagation angle of 89.5° (top panels of Fig. 5). The growth rates are weaker for $\cos^{-1}\left(\hat{\mathbf{k}}\cdot\hat{\mathbf{B}}_0\right) = 85.0°$ than they are for $\cos^{-1}\left(\hat{\mathbf{k}}\cdot\hat{\mathbf{B}}_0\right) = 89.5°$. In all the results presented, the NBI protons have no initial velocity along the background magnetic, for both propagation angles. Spatio-temporal Fourier transforms of the excited fields are shown in Fig. 6, where the four panels correspond to the cases in Fig. 5. The simulated power spectra shown in Fig. 7 correspond again to the four panels in Figs. 5 and 6. These spectra, including also those in the bottom panels of Fig. 8, are constructed from Fig. 6 as follows: we compute the spatio-temporal fast Fourier transform (FFT) of the z-component of the fluctuating part of the magnetic field, δB_z, (Fig. 6), and then sum over wavenumbers between $k = 0$ and $k = 25\Omega_H/V_A$. Fig. 8 suggests that our simulations capture the observed ICE spectral properties shown in Fig. 2, in both the sub-Alfvénic and super-Alfvénic NBI regimes in LHD. The propagation angle is 89.5° in the simulated spectra reproduced at the bottom of Fig. 8 because they saturate much quicker while the 85.0° suggests that ICE can be emitted away from pure perpendicular propagation. All the simulated spectra in Fig. 7 show strong excitation at multiple successive proton cyclotron harmonics; and the ICE signal in the simulations is a hundred to a thousand times more intense than the thermal noise. Decreasing the angle between k and

B_0 shows preferential excitation at lower harmonics, as well as well as longer timescales for mode excitations, see Fig. 6. Since the power spectra at the bottom panels are averaged over a much longer time periods, high spectral resolution is achieved that translates into the thick curves. The similar intensities on the right panels are due to comparable NBI proton densities. Conversely, the proton beams densities differ by an order of magnitude on the left panels to saturate the MCI in a tractable computing time, whence the different intensities. In Fig. 9, we plot the time evolution of the spatial FFT of $\delta B_z^2/B_0^2$. There is a one-to-one mapping between the excited k-values and the cyclotron harmonics $\ell\Omega_H$, inferred from the dispersion relation of the fast Alfvén wave using information in Fig. 6. Thus by plotting the time evolution of the distribution of energy across wavenumbers, as in Figure 9, we can identify the time sequence in which specific cyclotron harmonics in the simulated ICE spectrum are excited. A notable feature of Fig. 9 is the late excitation of the spectral peak at the fundamental cyclotron frequency of the protons in the nonlinear phase.

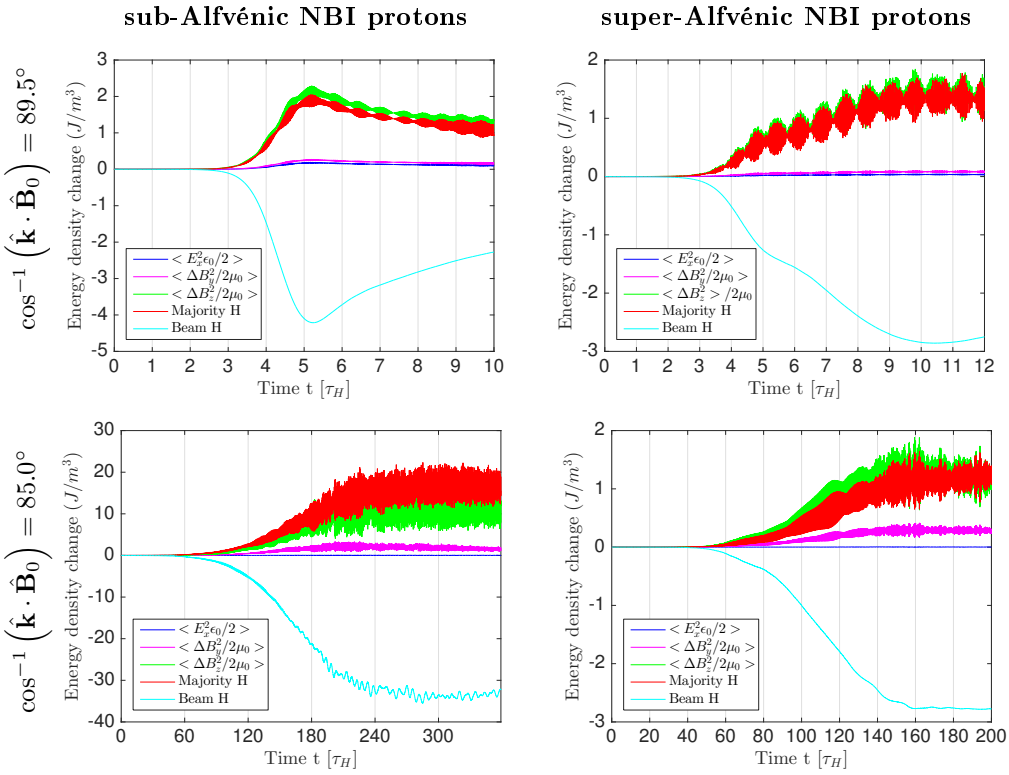

Figure 5: Time evolution (horizontal axis, in units of proton gyroperiods τ_H) of the energy density of different field components and particle populations in four PIC-hybrid simulations. Left panels are for LHD hydrogen plasma 79126 with sub-Alfvénic 40 keV NBI protons, for which $v_{NBI}/V_A = 0.872$. Right panels are for LHD hydrogen plasma 79003 with super-Alfvénic 36.5 keV NBI protons for which $v_{NBI}/V_A = 1.125$. Top panels are for propagation angle of $\mathbf{k}$ with respect to $\mathbf{B}_0$ of 89.5°. Bottom panels are for propagation angle 85°. Concentration $\xi = n_{NBI}/n_e$ is chosen at a level that gives rise to saturation of the MCI within the simulation run time: $\xi = 5 \times 10^{-4}$ at top left and bottom right; $\xi = 7.5 \times 10^{-4}$ at top right; and $\xi = 5 \times 10^{-3}$ at bottom left. Red trace: bulk protons. Cyan: NBI protons. Green z-component and magenta y-component of the fluctuating part of the magnetic field. Dark blue: x-component of the electric field. The excitation of the y-component of the magnetic field is due to the NBI protons that have a velocity component along the z direction, while $\mathbf{k}$ is along the 1D simulation domain ($\hat{\mathbf{x}}$ direction). The NBI protons typically release 10-15% of their energy to the background protons and to the electric and magnetic fields. Saturation of the instability occurs after $\approx 1\mu$s to 100μs. This time is similar to the time window used to compute the LHD power spectra (see Fig 2. of Ref. [11]).

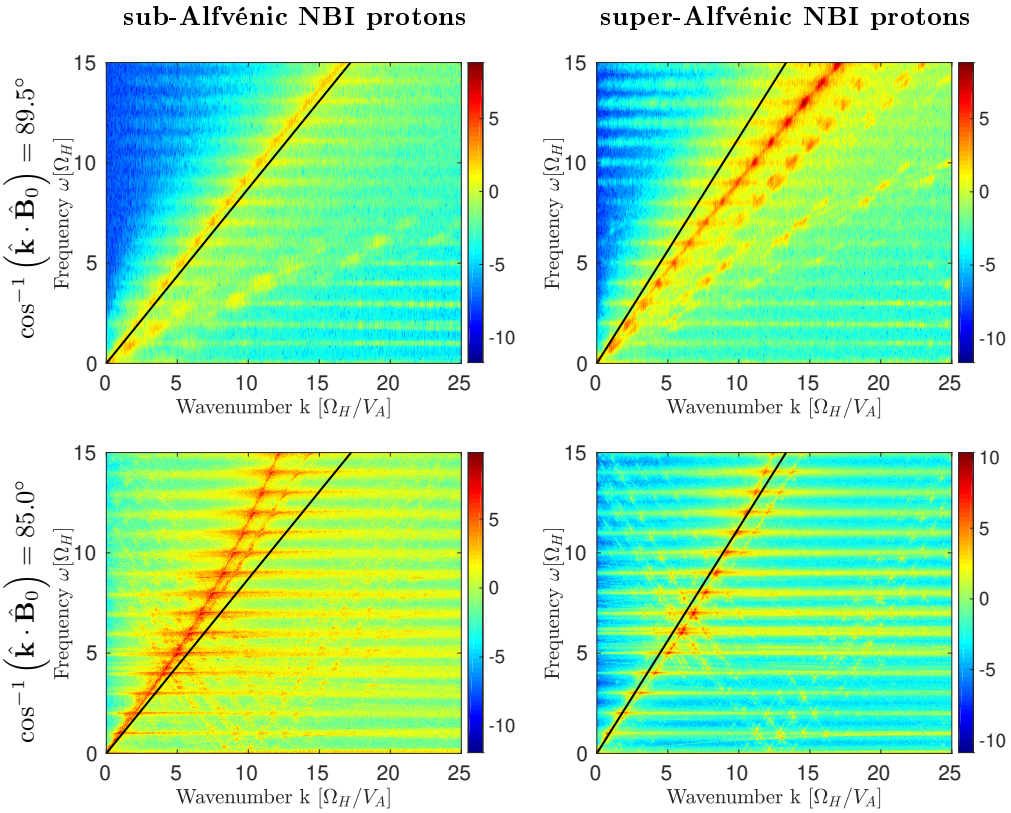

Figure 6: Spatio-temporal Fourier transform of the z-component of the fluctuating part of the magnetic field, δB_z, in the four PIC simulations whose energy evolution is shown in the corresponding panels of Fig. 5. The transform is calculated across the spatial domain and averaged over the simulation duration; magnitude is plotted on a $\log_{10}$ colour scale. The left and right pairs of panels correspond to simulations that have different values of NBI proton injection speed v_{NBI} compared to the Alfvén speed V_A, in the LHD plasma near the NBI injection point: (left) $v_{NBI}/V_A = 0.870$, (right) $v_{NBI}/V_A = 1.125$. Bright spots at sequential proton cyclotron harmonics along the fast-Alfvén branch result from the MCI, driven by NBI protons, for waves propagating in the $\hat{\mathbf{x}}$ direction, almost perpendicular to the background magnetic field. The dark trace corresponds to $\omega = kv_{NBI}$ and lies either above or below $\omega = kV_A$, which defines the boundary between regions of $(\omega, \mathbf{k})$ space that can in principle resonate with sub-Alfvénic or super-Alfvénic NBI protons. The excitations occur along the fast Alfvén branch and preferentially close to modes satisfying $\omega = kv_{NBI}$.

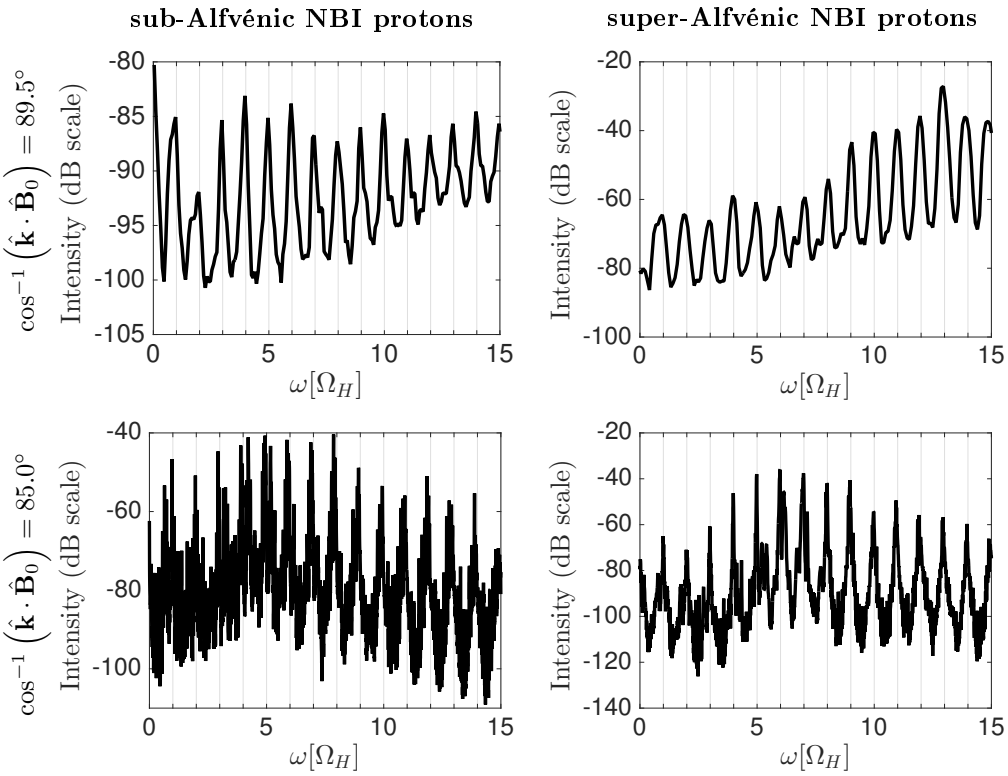

Figure 7: Power spectra of the fluctuating z-component of the magnetic field in the four PIC-hybrid simulations whose energy evolution and spatiotemporal Fourier transforms are shown in the corresponding panels of Fig. 5 and Fig 6. respectively. Power spectra are obtained using different orientations of the background magnetic field with respect to the 1D3V simulation, which defines the direction of $\mathbf{k}$. Power spectra are obtained by taking the spatio-temporal Fourier transform $\delta B_z(t) = B_z(t) - B_{0,z}$, averaged over the simulation duration and summed between $k = 0$ and $k = 25\Omega_H/V_A$. Peaks at multiple successive proton cyclotron harmonics are captured.

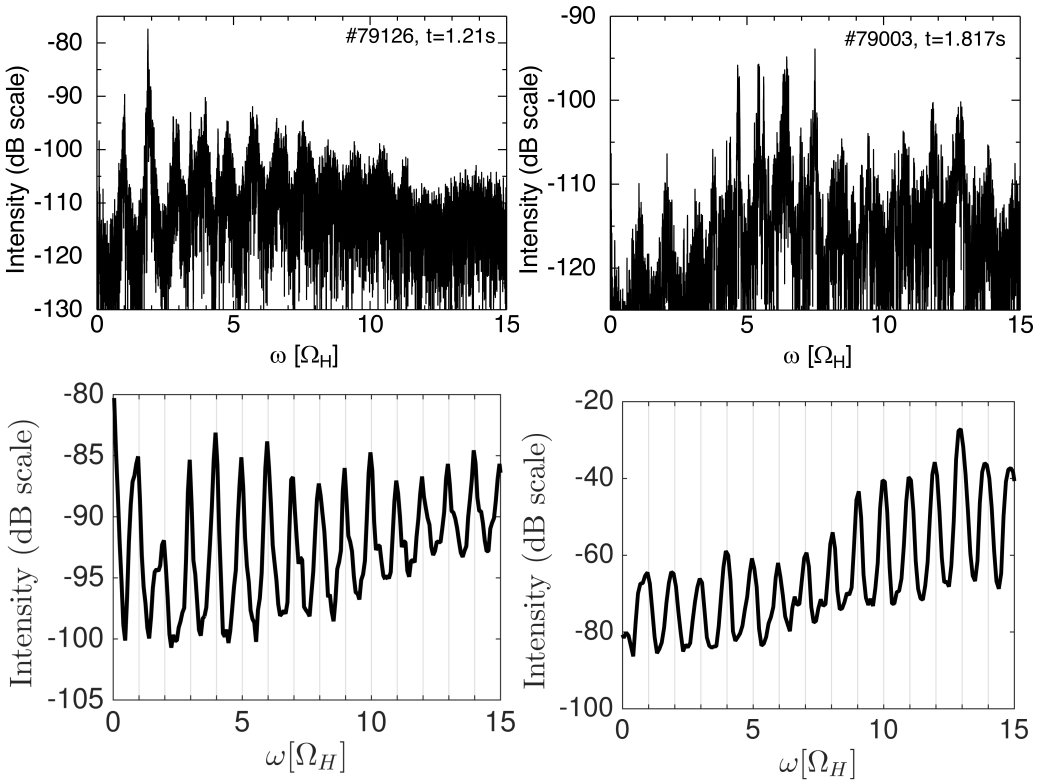

Figure 8: Comparison of measured and simulated ICE spectra, plotted on dB scales. Top panels: measured LHD ICE power spectra during sub-Alfvénic (left) and super-Alfvénic (right) perpendicular proton NBI, reproducing Fig. 2. Bottom panels: power spectra of $\delta B_z^2/B_0^2$ obtained from our PIC-hybrid simulations for parameters corresponding to LHD plasmas 79126 (left) and 79003 (right), see Table 1, reproducing the top two panels of Fig. 7.

5 Identification of the excitation process for NBI proton driven ICE in LHD plasmas

The frequencies of the modes excited by ICE in our simulations typically range from $\omega \approx 5\Omega_H$ to $\approx 45\Omega_H$. We focus primarily on modes up to $\omega \approx 15\Omega_H$, marginally stable and unstable, because this is upper frequency limit of the experimental measurements. These modes are electromagnetic and lie on the fast Alfvén branch, so that ω and k are related by $\omega \approx V_A k$, where V_A is the Alfvén speed. In our simulations, we consider waves propagating nearly perpendicular to the local background magnetic field. Such waves can leave an MCF plasma, propagating radially, and be detected beyond it. The simulation outputs encapsulated in Fig. 9 enable us to infer the rate at which the energy in a given cyclotron harmonic spectral peak grows over time. It is particularly helpful to calculate this during the early phase of growth, because this eanbles quantitative comparison with counterpart linear growth rates obtained from analytical theory. We denote the early phase growth rate inferred from the simulations at the ℓth harmonic by γ_ℓ. This we shall compare with the corresponding scaling of analytical linear growth rate for the MCI, $\gamma_{lin}(\ell)$, defined [36] by equations 6 and 7 below. Equation 8 shows that $\gamma_{lin} \sim \xi^{1/2}$; hence Figs. 10 and 11 compare early phase simulation outputs with linear theory by plotting γ_ℓ versus $\xi^{1/2}$ for

multiple simulations at a propagation angle of 89.5°, focusing on $\ell = 11$ and $\ell = 12$ for sub-Alfvénic NBI LHD plasma 79126 and super-Alfvénic NBI LHD plasma 79003 respectively. The agreement shown is good; this further confirms the role of the MCI in our simulations and, by extension, the LHD experiments. Figures 10 and 11 are obtained as follows. The Alfvén dispersion relation provides a one-to-one mapping between the excited ω modes and the excited k modes. In addition, our simulations use an initially uniform density for both the NBI protons and the background plasma, and the domain has periodic boundary conditions. This means there is neither loss of information, nor need for windowing, when taking spatial Fourier transforms of the electric and magnetic fields. We may therefore compute the growth rates of k-modes by taking the spatial Fourier transform of $B_z(x,t)$, which we perform for a propagation angle of 89.5°, leading to $B_z(k,t)$ as shown on the top panels in Fig. 9. One selects an ω-mode at $\omega = \ell\Omega_H, 5 \leq \ell \leq 15$, to which a unique k-mode, $k = k_{\ell\Omega_H}$ is associated through the dispersion relation as in Fig. 6. The time evolution of $B_z\left(k_{\ell\Omega_H}, t\right)$ is then plotted and best fits are constructed to extract the empirical growth rate γ_ℓ of this mode, as described below. This approach is convenient because it does not require transformations from the time domain. Once $B_z\left(k_{\ell\Omega_H}, t\right)$ is calculated, we identify the interval $[t_0, t_1]$ over which the initial exponential growth phase takes place in our simulations. A primary objective is to

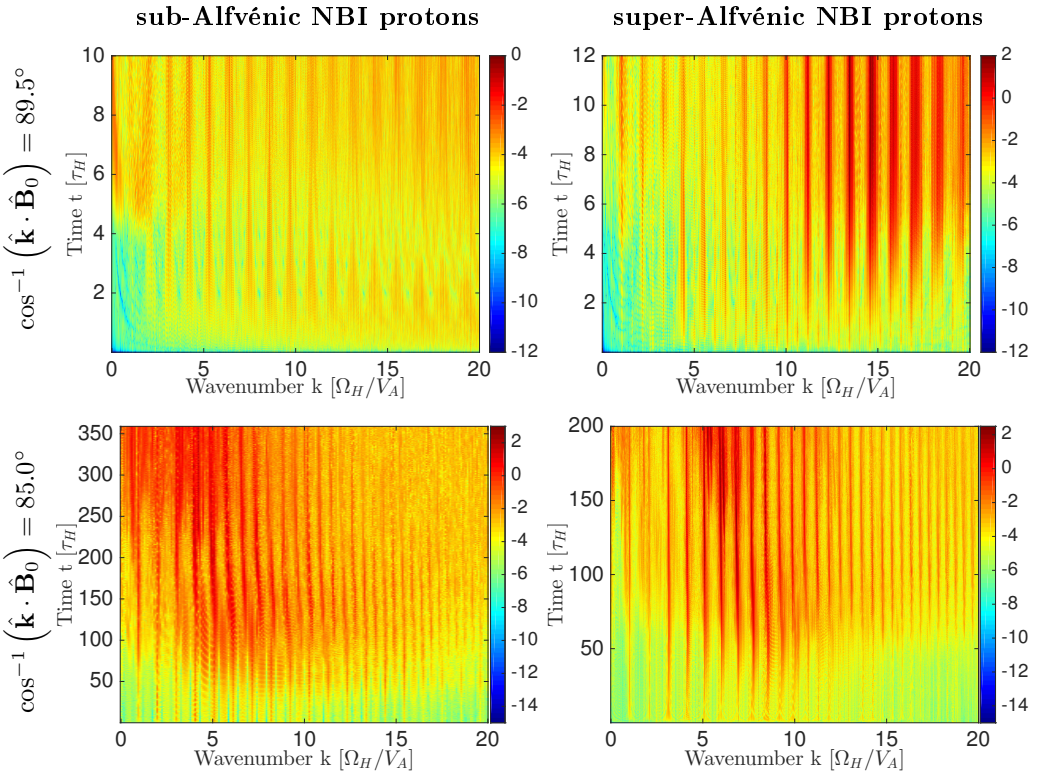

Figure 9: Time evolution (vertical axis, in units of proton gyroperiods τ_H) of the spatial Fourier transform of the z-component of the fluctuating magnetic field δB_z in the four PIC simulations whose energy evolution, spatiotemporal Fourier transforms, and ICE spectra are shown in the corresponding panels of Fig. 5, Fig. 6 and Fig. 7 respectively. Magnitude is plotted on a log 10 colour scale. Wavenumbers are normalized to the proton skin depth Ω_H/V_A. The vertical bands correspond to the most strongly excited wavenumbers, which can be mapped to successive proton cyclotron harmonics using information in Fig 6. The modes excited earliest in the simulations are the most strongly linearly unstable ones, starting at cyclotron harmonic $\ell = 5$, approximately.

quantify the scaling of the initial growth rate inferred from simulations, γ_ℓ, with NBI proton number density. This can be compared to the scaling

given by the corresponding analytical expression $\gamma_{lin(\ell)}$ obtained from linear instability theory, specifically the MCI [38], see below. We find the duration of this initial exponential growth phase in the simulations to be $\approx 1.0\tau_H$ for the fastest-growing modes, while the slowest-growing ones unfold over $\approx 20\tau_H$. We perform multiple fits of $B_z\left(k_{\ell\Omega_H}, t\right)$ between $[t_{1/2}-n\Delta t, t_{1/2}-n\Delta t]$ where: $t_{1/2}$ is at the centre of $[t_0, t_1]$, which are the start and end times of the initial exponential growth; $\Delta t \approx 0.001\Omega_H$; and n varies between 1 and n_{max}, such that $[t_{1/2} - n_{max}\Delta t, t_{1/2} + n_{max}\Delta t]$ is the smallest interval to contain $[t_0, t_1]$. This yields a family of n growth rates $\gamma_{\ell,n}, 1 \leq n \leq n_{max}$ for a given mode at $\omega = \ell\Omega_H$. We take the mean of the individual best fits as the growth rate value $\gamma_\ell = \bar{\gamma}_{\ell,n}$, and define the associated error $\Delta\gamma_\ell = \sigma\left(\gamma_{\ell,n}\right)$, where the bar and sigma respectively represent the average and the standard deviation. The average and variance are taken between $n_{min} \leq n \leq n_{max}$, where n_{min} satisfies $n_{min}\Delta t \geq 0.5\tau_H/\ell$. That is, computation of the average starts from Δt corresponding to half an oscillation of the unstable ℓth mode. This enables us to use the same value of Δt for each cyclotron harmonic ℓ. The procedure described above enables us to calculate growth rates denoted γ_ℓ for the ℓth harmonic during the early phase of simulations. These are next compared with the scaling of the analytical expressions for the corresponding

growth rate $\gamma_{lin}(\ell)$ of the MCI, notably Eq. 36 of [38] which reads:

$$\frac{\gamma_{lin}(\ell)}{\Omega_H} = \frac{\Delta\omega}{\omega_0} = \sqrt{2}\frac{V_A}{v_{NBI}}\frac{\omega_{p,NBI}}{\omega_{pi}}\chi_0 = \sqrt{2}\frac{V_A}{v_{NBI}}\sqrt{\frac{n_{NBI}}{n_e}}\chi_0 \tag{6}$$

Here $\omega_{p,NBI}$ and ω_{pi} are the plasma frequencies of the NBI protons and of the bulk protons respectively, and v_{NBI} is again the initial velocity of NBI protons. We define

$$\chi_0^2 = \Pi_{x,x} - \frac{2i\omega\Omega_H}{V_A^2k^2}\Pi_{x,y} + \frac{\Omega_H^2}{V_A^2k^2}\Pi_{y,y} \tag{7}$$

where $\Pi_{x,x}$, $\Pi_{x,y}$ and $\Pi_{y,y}$ are the functions of $z_{NBI} = kv_{NBI}/\Omega_H$ of given in the appendix of [38]. Near resonance, $\omega_0 = V_Ak = \ell\Omega_H$ and $z_{NBI} = \ell v_{NBI}/V_A$. For a given mode ℓ, if all parameters are kept fixed except for the NBI proton density $\xi = n_{NBI}/n_e$, Eq. 6 yields the scaling

$$\frac{\gamma_{lin}(\ell)}{\Omega_H} = \frac{\Delta\omega}{\omega_0} = \alpha_\ell\sqrt{\xi} \tag{8}$$

as in Fig. 11, where

$$\alpha_\ell \equiv \sqrt{2}\frac{V_A}{v_{NBI}}\chi_0 \tag{9}$$

which depends on ℓ solely.

We test the hypothesis that $\gamma_\ell \simeq \gamma_{lin}(\ell)$ by running multiple simulations for different values of the beam proton density ratio ξ, with all other pa-

rameters kept fixed. The computed growth rates at early times γ_ℓ for a given mode ℓ, obtained by mean of $B_\xi\left(k_{\ell\Omega_H}, t\right)$ as appeared in Fig. 9, are then plotted against $\sqrt{\xi}$, in line with the analytical scaling of $\gamma_{lin}\left(\ell\right)$ [5, 38] in Eq. 8 as shown in Figure 10. This shows congruence between the early phase of collective relaxation of the NBI ion population in our first principles PIC-hybrid simulations, and the analytical theory of the linear stage of the MCI. It tends to confirm that the resulting ICE spectra can be understood in terms of the MCI, which our simulations extend into the analytically inaccessible nonlinear regime, for both sub-Alfvénic and super-ALfvénic NBI proton populations.

The procedure is now applied accross multiple harmonic modes with the results shown Fig. 11.

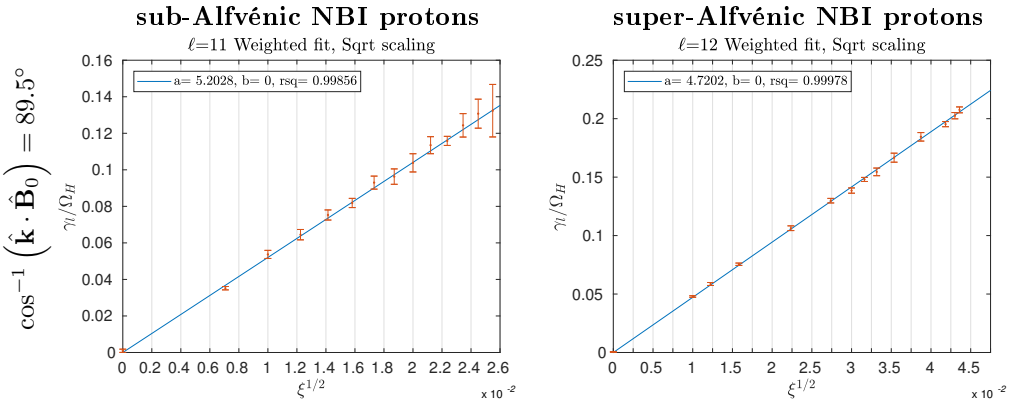

Figure 10: Linear fit of early phase growth rate γ_ℓ inferred from the simulations at an angle of 89.5°, normalized to Ω_H, against the square root of $\xi = n_{NBI}/n_e$, subject to the constraint that for a zero density beam, the line should intersect the origin. It is evident that the ICE growth rate γ_ℓ/Ω_H scales as $\sqrt{\xi}$. Left panel is for cyclotron harmonic mode $\ell = 11$ of the excited wave in the ICE emitting region of LHD plasma 79126 with locally sub-Alfvénic 40keV NBI protons, and each point is for a value of ξ between 0.5×10^{-4} and 7.5×10^{-4}. Right panel is for cyclotron harmonic mode $\ell = 12$ of the excited wave in the ICE emitting region of LHD plasma 79003 with locally super-Alfvénic 36.5keV NBI protons, and the values of ξ are between 1×10^{-4} and 2×10^{-3}.

As in Fig. 10, in Fig. 11 we plot the dependence of the growth rate γ_ℓ of the fields, calculated at early times in multiple simulations, on NBI concentration ξ in each simulation. The computations are performed for parameters corresponding to LHD plasmas 79126 and 79003. In both scenarios, the propagation angle between $\mathbf{B}_0$ and $\mathbf{k}$ is 89.5°. The left pair of

panels in Fig. 11 corresponds to the collapsed plot which recasts Eq. 8 as

$$\left(\gamma_{lin}\left(\ell\right)/\Omega_H\right)/\alpha_\ell = \sqrt{\xi} \tag{10}$$

Namely, the quantity $\left(\gamma_{lin}\left(\ell\right)/\Omega_H\right)/\alpha_\ell$ is proportional to $\sqrt{\xi}$, whence the straight line obtained independently of the mode number ℓ. The right pair of panels in Fig. 11 instead reformulates Eq. 8 as

$$\left(\gamma_{lin}\left(\ell\right)/\Omega_H\right)/\sqrt{\xi} = \alpha_\ell \tag{11}$$

This implies that for a fixed mode value ℓ, the quantity $\left(\gamma_{lin}\left(\ell\right)/\Omega_H\right)/\sqrt{\xi}$ is independent of ξ and equals a constant that depends on ℓ solely. We translate that constant such that it equals $\alpha'_\ell = \ell$. Figure 11 strongly suggests that in general $\gamma_\ell \sim \xi^{1/2}$ in our simulations, across an extended range of modes. This dependence is the same as for growth rates from linear analysis of the MCI [38], and from previous simulations e.g Fig. 3 of [66]. Additional linear and cubic root scaling tests have been performed, and F-test statistics [96] applied with a 99% significance further confirm the square root scaling.

We have also investigated, through PIC-hybrid simulations, the collective relaxation of NBI proton populations that have artificially enhanced sub- and super-Alfvénic characteristics under the LHD plasma conditions already considered. We have run multiple simulations of a sub-Alfvénic fast proton

population of 25keV, for which $v_{NBI}/V_A = 0.7$ under LHD plasma 79126 conditions, as well as simulations with a 56keV super-Alfvénic fast proton beam, for which $v_{NBI}/V_A = 1.4$ under LHD 79003 plasma edge conditions. The same conclusions are obtained.

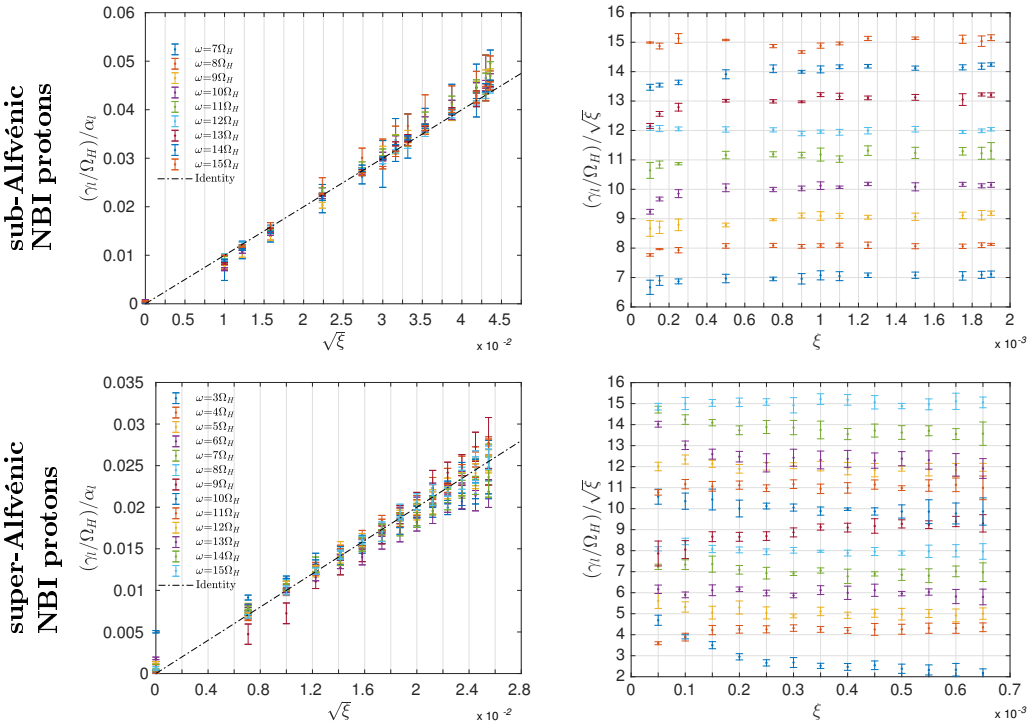

Figure 11: Dependence of early phase growth rates γ_ℓ in simulations at an angle of 89.5° with different NBI ion concentration ξ, obtained accross multiple cyclotron harmonics ℓ. Top and bottom pairs of panels correspond to LHD plasmas 79003 and 79126 respectively. Left: collapsed plot of $(\gamma_\ell/\Omega_H)/\alpha_\ell$, versus ξ. Here $\gamma_\ell = \gamma_\ell(\xi)$ is the growth rate inferred from the simulations for mode number ℓ, and depends on the relative NBI density ξ at the ICE location, and α_ℓ is the calculated slope from the best linear fit of γ_ℓ as a function of $\sqrt{\xi}$ for a given mode ℓ (see Fig. 10). Right: translated compensated plot of the quantity $(\gamma_\ell/\Omega_H)/\sqrt{\xi}$ versus ξ, with γ_ℓ inferred from simulations. If the simulation outputs match the linear theory of the MCI, we expect $\gamma_\ell/\Omega_H = \alpha_\ell\sqrt{\xi}$ as in Eq. 8. In this case, it follows that $(\gamma_\ell/\Omega_H)/\sqrt{\xi} = \alpha_\ell$, a quantity that does not depend on ξ, but on the mode value ℓ only. This outcome is reflected by the sequence of horizontal lines in to the compensated plot. The values of ξ span one order of magnitude, between 10^{-4} and 10^{-3}. Together, these graphs show that, within modest error bars, $\gamma_\ell \propto \sqrt{\xi}$.

6 Conclusions

The measured ion cyclotron emission (ICE) spectra (Fig. 2) from LHD hydrogen plasmas with both sub-Alfvénic and super-Alfvénic perpendicular proton NBI have been successfully simulated (Fig. 7) using a first principles approach. Direct numerical simulation of kinetic ions (bulk protons and minority energetic NBI protons) and fluid electrons using a 1D3V PIC-hybrid code captures the self-consistent Maxwell-Lorentz dynamics of the plasma and fields. It is observed from the Fourier transformed code outputs that the dominant physical process driving this ICE is the magnetoacoustic cyclotron instability (MCI). The results presented here suggest there is a unified basic emission mechanism, corresponding to the nonlinear MCI, responsible for the main features of ICE in both tokamak and LHD plasmas. The spontaneously excited electric and magnetic fields in our simulations, which are carried out in local slab geometry, correspond to the fast Alfvén wave. This work helps establish a baseline for future energetic particle experiments in LHD, where magnetic geometry and toroidal eigenfunctions [50] may play a larger role. ICE links beam ion physics in LHD to fusion-born ion physics in tokamaks, and has significant diagnostic potential.

7 Acknowledgments

This work has been carried out within the framework of the EUROfusion Consortium and has received funding from the Euratom research and training programme 2014-2018 and 2019-2020 under grant agreement No 633053. The work received support from the RCUK Energy Programme [grant number EP/P012450/1], NIFS budget ULHH029 and from NRF Korea grant no. 2014M1A7A1A03029881. The views and opinions expressed herein do not necessarily reflect those of the European Commission. ROD acknowledges the hospitality of Kyushu University. BCGR acknowledges helpful discussion with Dr. Carbajal-Gomez.

References

[1] R. O. Dendy and K.G. McClements. Ion cyclotron emission from fusion-born ions in large tokamak plasmas: a brief review from JET and TFTR to ITER. *Plasma Phys. Control. Fusion*, 57, 2015. doi: 10.1088/0741-3335/57/4/044002. URL http://dx.doi.org/10.1088/0741-3335/57/4/044002.

[2] N. N. Gorelenkov. Ion cyclotron emission studies: Retrospects and prospects. *Plasma Physics Reports*, 42(5):430–439, 2016. ISSN 1562-6938. doi: 10.1134/S1063780X16050044. URL http://dx.doi.org/10.1134/S1063780X16050044.

[3] TFR Equipe. High-power neutral injection and ion power balance in TFR. *Nuclear Fusion*, 18(9):1271, 1978.

[4] DK Bhadra, SC Chiu, D Buchenauer, and D Hwang. Electromagnetic emission from a neutral-beam-injected plasma. *Nuclear Fusion*, 26(2): 201, 1986.

[5] G.A. Cottrell and R. O. Dendy. Superthermal Radiation from Fusion Products in JET. *Physical Review Letters*, 60:33–36, 1988.

[6] S Cauffman and R Majeski. Ion cyclotron emission on the Tokamak

Fusion Fest Reactor. *Review of Scientific Instruments*, 66(1):817–819, 1995.

[7] H Kimura, Y Kusama, M Saigusa, GJ Kramer, K Tobita, M Nemoto, T Kondoh, T Nishitani, O Da Costa, T Ozeki, et al. Alfvén eigenmode and energetic particle research in JT-60U. *Nuclear Fusion*, 38(9):1303, 1998.

[8] R. D'Inca M. García Muñoz, G. Tardini, J. M. Noterdaeme, and the ASDEX Upgrade Team. Characteristics of Ion Cyclotron Emission on ASDEX Upgrade. 38th EPS Conference on Plasma Physics, 2011. URL http://ocs.ciemat.es/EPS2016PAP/pdf/O2.101.pdf.

[9] Shekar G Thatipamula, GS Yun, J Leem, Hyeon Keo Park, KW Kim, T Akiyama, and SG Lee. Dynamic spectra of radio frequency bursts associated with edge-localized modes. *Plasma Physics and Controlled Fusion*, 58(6):065003, 2016.

[10] WW Heidbrink, ME Austin, RK Fisher, M Garcia-Munoz, G Matsunaga, GR McKee, RA Moyer, CM Muscatello, M Okabayashi, DC Pace, et al. Characterization of off-axis fishbones. *Plasma Physics and Controlled Fusion*, 53(8):085028, 2011. doi: 10.1088/0741-3335/53/8/085028. URL http://dx.doi.org/10.1088/0741-3335/53/8/085028.

[11] Kenji Saito, H Kasahara, T Seki, R Kumazawa, Takashi Mutoh, Tsuguhiro Watanabe, Fujio Shimpo, Goro Nomura, Masaki Osakabe, M Ichimura, et al. Measurement of ion cyclotron emissions by use of ICRF heating antennas in LHD. *Fusion Engineering and Design*, 84 (7):1676–1679, 2009.

[12] K. Saito, R. Kumazawa, T. Seki, H. Kasahara, G. Nomura, F. Shimpo, H. Igami, M. Isobe, K. Ogawa, K. Toi, M. Osakabe, M. Nishiura, T. Watanabe, S. Yamamoto, M. Ichimura, T. Mutoh, and LHD Experiment Group. Measurement of ion cyclotron emissions by using high frequency magnetic probes in the LHD. *Plasma Science and Technology*, 15, 2013. doi: 10.1088/1009-0630/15/3/03. URL http://dx.doi.org/10.1088/1009-0630/15/3/03.

[13] AG Shalashov, EV Suvorov, LV Lubyako, H Maassberg, et al. NBI-driven ion cyclotron instabilities at the W7-AS stellarator. *Plasma Physics and Controlled Fusion*, 45(4):395, 2003.

[14] G.A. Cottrell, V.P. Bhatnagar, O. Da Costa, R.O. Dendy, J. Jacquinot, K.G. McClements, D.C. McCune, M.F.F. Nave, P. Smeulders, and D.F.H. Start. Ion cyclotron emission measurements during JET deuterium-tritium experiments. *Nuclear Fusion*, 33:1365–1387, 1993.

doi: 10.1088/0029-5515/33/9/I10. URL http://iopscience.iop.org/0029-5515/33/9/I10/.

[15] S. Cauffman, R. Majeski, K. G. McClements, and R. O. Dendy. Alfvenic behaviour of alpha particle driven ion cyclotron emission in TFTR. *Nuclear Fusion*, 35:1597–1602, 1995. URL http://iopscience.iop.org/0029-5515/35/12/I22.

[16] R. O. Dendy, K. G. McClements, C.N. Lashmore Davies, G. A. Cottrell, R. Majeski, and S. Cauffman. Ion cyclotron emission due to collective instability of fusion products and beam ions in TFTR and JET. *Nuclear Fusion*, 35:1733–1742, 1995. URL http://0-iopscience.iop.org.pugwash.lib.warwick.ac.uk/article/10.1088/0029-5515/35/12/I38/pdf.

[17] K.G. McClements, C. Hunt, and R. O. Dendy. Ion Cyclotron Emission from JET D-T Plasmas. *Phys. Rev. Lett*, 82:2099–2102, 1999. URL http://0-journals.aps.org.pugwash.lib.warwick.ac.uk/prl/pdf/10.1103/PhysRevLett.82.2099.

[18] KE Thome, DC Pace, RI Pinsker, O Meneghini, CA del Castillo, and Y Zhu. Radio frequency measurements of energetic-particle-driven emission using the ion cyclotron emission diagnostic on the DIII-D tokamak. *Review of Scientific Instruments*, 89(10):10I102, 2018.

[19] R Ochoukov, V Bobkov, B Chapman, R Dendy, M Dunne, H Faugel, M García-Muñoz, B Geiger, P Hennequin, KG McClements, et al. Observations of core ion cyclotron emission on ASDEX Upgrade tokamak. *Review of Scientific Instruments*, 89(10):10J101, 2018.

[20] K.G. McClements, R. D'Inca, R. O. Dendy, L. Carbajal, S.C. Chapman, J.W.S. Cook, R.W. Harvey, W.W. Heidbrink, and S.D. Pinches. Fast particle-driven ion cyclotron emission (ICE) in tokamak plasmas and the case for an ICE diagnostic in ITER. *Nuclear Fusion*, 55(4):043013, 2015.

[21] M Osakabe, S Yamamoto, K Toi, Y Takeiri, S Sakakibara, K Nagaoka, K Tanaka, K Narihara, LHD Experimental Group, et al. Experimental observations of enhanced radial transport of energetic particles with Alfvén eigenmode on the LHD. *Nuclear Fusion*, 46(10):S911, 2006.

[22] K Toi, K Ogawa, M Isobe, M Osakabe, Donald A Spong, and Yasushi Todo. Energetic-ion-driven global instabilities in stellarator/helical plasmas and comparison with tokamak plasmas. *Plasma Physics and Controlled Fusion*, 53(2):024008, 2011.

[23] SE Sharapov, B Alper, HL Berk, DN Borba, BN Breizman, CD Challis, IGJ Classen, EM Edlund, Jacob Eriksson, A Fasoli, et al. Energetic

particle instabilities in fusion plasmas. *Nuclear Fusion*, 53(10):104022, 2013.

[24] Y Todo, MA Van Zeeland, and WW Heidbrink. Fast ion profile stiffness due to the resonance overlap of multiple Alfvén eigenmodes. *Nuclear Fusion*, 56(11):112008, 2016.

[25] VS Belikov and Ya I Kolesnichenko. *Soviet Physics Technical Physics*, 20:1146, 1976.

[26] L. Carbajal, R. O. Dendy, S.C. Chapman, and J.W.S. Cook. Linear and nonlinear physics of the magnetoacoustic cyclotron instability of fusion born-ions in relation to ion cyclotron emission. *Physics of Plasmas*, 21 (1):012106, 2014.

[27] Charles Galton Darwin. The dynamical motions of charged particles. *The London, Edinburgh, and Dublin Philosophical Magazine and Journal of Science*, 39(233):537–551, 1920.

[28] TD Arber, Keith Bennett, CS Brady, A Lawrence-Douglas, MG Ramsay, NJ Sircombe, P Gillies, RG Evans, Holger Schmitz, AR Bell, et al. Contemporary particle-in-cell approach to laser-plasma modelling. *Plasma Physics and Controlled Fusion*, 57(11):113001, 2015.

[29] JWS Cook, SC Chapman, and RO Dendy. Electron current drive by

fusion-product-excited lower hybrid drift instability. *Physical Review Letters*, 105(25):255003, 2010.

[30] J.W.S. Cook, R. O. Dendy, and S.C. Chapman. Particle-in-cell simulations of the magnetoacoustic cyclotron instability of fusion-born alpha particles in tokamak plasmas. *Plasma Physics and Controlled Fusion*, 55(6):065003, 2013.

[31] JWS Cook, RO Dendy, and SC Chapman. Stimulated emission of fast Alfvén waves within magnetically confined fusion plasmas. *Physical Review Letters*, 118(18):185001, 2017.

[32] B Chapman, RO Dendy, KG McClements, SC Chapman, GS Yun, SG Thatipamula, and MH Kim. Sub-microsecond temporal evolution of edge density during edge localized modes in KSTAR tokamak plasmas inferred from ion cyclotron emission. *Nuclear Fusion*, 57(12):124004, 2017.

[33] Benjamin Chapman, Richard O Dendy, Sandra C Chapman, Kenneth G McClements, Gunsu S Yun, Shekar Goud Thatipamula, and Minho Kim. Nonlinear wave interactions generate high-harmonic cyclotron emission from fusion-born protons during a KSTAR ELM crash. *Nuclear Fusion*, 58(9):096027, 2018.

[34] R. O. Dendy, K. G. McClements, C.N. Lashmore Davies, R. Majeski, and S. Cauffman. A mechanism for fusion beam-driven excitation of ion cyclotron waves in the Tokamak Fusion Test Reactor. *Physics of Plasmas*, 1:3407–3413, 1994. doi: 10.1063/1.870489. URL http://dx.doi.org/10.1063/1.870489.

[35] P. Schild, G.A. Cottrell, R. O. Dendy, and K.G. McClements. Sawtooth oscillations in ion cyclotron emission from JET. *Nuclear Fusion*, 29(5): 834–839, 1989.

[36] GA Cottrell, VP Bhatnagar, O Da Costa, RO Dendy, J Jacquinot, KG McClements, DC McCune, MFF Nave, P Smeulders, and DFH Start. Ion cyclotron emission measurements during JET deuterium-tritium experiments. *Nuclear Fusion*, 33(9):1365, 1993.

[37] GA Cottrell. Identification of minority ion-cyclotron emission during radio frequency heating in the JET tokamak. *Physical Review Letters*, 84(11):2397, 2000.

[38] RO Dendy, Chris N Lashmore-Davies, and KF Kam. A possible excitation mechanism for observed superthermal ion cyclotron emission from tokamak plasmas. *Physics of Fluids B: Plasma Physics*, 4(12): 3996–4006, 1992.

[39] RO Dendy, CN Lashmore-Davies, and KF Kam. The magnetoacoustic cyclotron instability of an extended shell distribution of energetic ions. *Physics of Fluids B: Plasma Physics*, 5(7):1937–1944, 1993.

[40] RO Dendy, Kenneth George McClements, CN Lashmore-Davies, R Majeski, and S Cauffman. A mechanism for beam-driven excitation of ion cyclotron harmonic waves in the Tokamak Fusion Test Reactor. *Physics of Plasmas*, 1(10):3407–3413, 1994.

[41] RO Dendy, CN Lashmore-Davies, Kenneth George McClements, and GA Cottrell. The excitation of obliquely propagating fast Alfvén waves at fusion ion cyclotron harmonics. *Physics of plasmas*, 1(6):1918–1928, 1994.

[42] JET Team et al. Fusion energy production from a deuterium-tritium plasma in the JET tokamak. *Nuclear Fusion*, 32(2):187, 1992.

[43] JD Strachan, H Adler, P Alling, C Ancher, H Anderson, JL Anderson, D Ashcroft, Cris W Barnes, G Barnes, S Batha, et al. Fusion power production from TFTR plasmas fueled with deuterium and tritium. *Physical ReviewLetters*, 72(22):3526, 1994.

[44] S Cauffman, R Majeski, KG McClements, and RO Dendy. Alfvénic behaviour of alpha particle driven ion cyclotron emission in TFTR. *Nuclear Fusion*, 35(12):1597, 1995.

[45] M. Seki, M. Saigusa, M. Nemoto, K. Kusama, T. Tobita, M. Kuriyama, and K. Uehara. Observation of ion-cyclotron-wave instability caused by perpendicular neutral beam injection in the JT-60 tokamak. *Phys. Rev. Lett.*, 62:1989–1992, Apr 1989. doi: 10.1103/PhysRevLett.62.1989. URL https://link.aps.org/doi/10.1103/PhysRevLett.62.1989.

[46] E. G. Harris. Unstable plasma oscillations in a magnetic field. *Phys. Rev. Lett.*, 2:34–36, Jan 1959. doi: 10.1103/PhysRevLett.2.34. URL https://link.aps.org/doi/10.1103/PhysRevLett.2.34.

[47] W Kerner, D Borba, GTA Huysmans, F Porcelli, Stefaan Poedts, JP Goedbloed, and R Betti. Stability of global Alfven waves (TAE, EAE) in JET tritium discharges. *Plasma Physics and Controlled Fusion*, 36(5):911, 1994.

[48] P. Jacquet, G. Berger-By, V. Bobkov, T. Blackman, I. E. Day, F. Durodié, M. Graham, T. Hellsten, M.-L. Mayoral M. Laxaback, f, I. Monakhov, M. Nightingale, S. E. Sharapov, M. Vrancken, , and JET-EFDA contributors. Parasitic signals in the receiving band of the Sub-Harmonic Arc Detection system on JET ICRF Antennas. *AIP Conference Proceedings*, 1406:17, 2011.

[49] Kenneth G McClements, Alexandra Brisset, Benjamin Chapman, Sandra C Chapman, Richard O Dendy, Philippe Jacquet, Vasily Kiptily,

Mervi Mantsinen, and Bernard CG Reman. Observations and modelling of ion cyclotron emission observed in JET plasmas using a sub-harmonic arc detection system during ion cyclotron resonance heating. *Nuclear Fusion*, 58, 2018. doi: https://doi.org/10.1088/1741-4326/aace03.

[50] NN Gorelenkov and CZ Cheng. Excitation of alfvén cyclotron instability by charged fusion products in tokamaks. *Physics of Plasmas*, 2(6):1961–1971, 1995.

[51] Shoichi Sato, Makoto Ichimura, Yuusuke Yamaguchi, Makoto Katano, Yasutaka Imai, Tatsuya Murakami, Yuichiro Miyake, Takuro Yokoyama, Shinichi Moriyama, Takayuki Kobayashi, et al. Observation of ion cyclotron emission owing to DD fusion product H ions in JT-60U. *Plasma and Fusion Research*, 5:S2067–S2067, 2010.

[52] M Ichimura, H Higaki, S Kakimoto, Y Yamaguchi, K Nemoto, M Katano, M Ishikawa, S Moriyama, and T Suzuki. Observation of spontaneously excited waves in the ion cyclotron frequency range on jt-60u. *Nuclear Fusion*, 48(3):035012, 2008. doi: 10.1088/0029-5515/48/3/035012. URL http://dx.doi.org/10.1088/0029-5515/48/3/035012.

[53] M Ichimura, M Katano, Y Yamaguchi, S Sato, Y Motegi, H Muro, T Ouchi, S Moriyama, M Ishikawa, K Shinohara, et al. Study of ion

cyclotron emissions due to DD fusion product ions on JT-60U. Technical report, Geneva, 2008.

[54] T Suzuki, N Oyama, A Isayama, Y Sakamoto, T Fujita, S Ide, Y Kamada, O Naito, M Sueoka, S Moriyama, et al. Development of advanced operation scenarios in weak magnetic-shear regime on JT-60U. *Nuclear Fusion*, 49(8):085003, 2009.

[55] RO Dendy, Kenneth George McClements, CN Lashmore-Davies, GA Cottrell, R Majeski, and S Cauffman. Ion cyclotron emission due to collective instability of fusion products and beam ions in TFTR and JET. *Nuclear Fusion*, 35(12):1733, 1995.

[56] O Da Costa and D Gresillon. Ion cyclotron emission by spontaneous emission. Technical report, 1994.

[57] Rodolphe D'Inca. *Ion cyclotron emission on ASDEX Upgrade*. PhD thesis, Ludwig-Maximilians-Universitat Munchen, 2014.

[58] R Ochoukov, V Bobkov, H Faugel, H Fünfgelder, J-M Noterdaeme, and ASDEX Upgrade Team. A new b-dot probe-based diagnostic for amplitude, polarization, and wavenumber measurements of ion cyclotron range-of frequency fields on ASDEX Upgrade. *Review of Scientific Instruments*, 86(11):115112, 2015.

[59] JG Cordey, RJ Goldston, and DR Mikkelsen. A generalized sufficient condition for velocity-space stability of fusion product distributions and application to heating of DT tokamak reactors. *Nuclear Fusion*, 21(5): 581, 1981.

[60] D.C. Pace W.W. Heidbrink R.I. Pinsker M.A. Van Zeeland Y.B. Zhu. Ion Cyclotron Emission in the Presence of Beam Ion Losses. 43rd EPS Conference on Plasma Physics, 2016. URL http://ocs.ciemat.es.EPS2011PAP/pdf/P1.053.pdf.

[61] D. A. Spong, W. W. Heidbrink, C. Paz-Soldan, X. D. Du, K. E. Thome, M. A. Van Zeeland, C. Collins, A. Lvovskiy, R. A. Moyer, M. E. Austin, D. P. Brennan, C. Liu, E. F. Jaeger, and C. Lau. First direct observation of runaway-electron-driven whistler waves in tokamaks. *Phys. Rev. Lett.*, 120:155002, Apr 2018. doi: 10.1103/PhysRevLett.120.155002. URL https://link.aps.org/doi/10.1103/PhysRevLett.120.155002.

[62] K.E. Thome D.C. Pace R.I. Pinsker M.A. R. del Castillo Y. Zhu. Radio frequency measurements of energetic particle modes using the ion cyclotron emission diagnostic on the DIII-D tokamak. San Diego California, 2018. 22nd Topical Conference on High-Temperature Plasma Diagnostics.

[63] TC Luce. An analytic functional form for characterization and generation of axisymmetric plasma boundaries. *Plasma Physics and Controlled Fusion*, 55(9):095009, 2013.

[64] Minho Kim, Shekar G Thatipamula, Jieun Lee, Minjun J Choi, Hyeon K Park, Tsuyoshi Akiyama, and Gunsu S Yun. Distinct stages of radio frequency emission at the onset of pedestal collapse in KSTAR H-mode plasmas. *arXiv preprint arXiv:1803.09376*, 2018.

[65] K. G. McClements, R. O. Dendy, C.N. Lashmore Davies, G. A Cottrell, S. Cauffman, and R. Majeski. Interpretation of ion cyclotron emission from subAlfvénic fusion products in the Tokamak Fusion Test Reactor. *Physics of Plasmas*, 3:543–553, 1995. doi: 10.1063/1.871881. URL http://dx.doi.org/10.1063/1.871881.

[66] L Carbajal, RO Dendy, Sandra C Chapman, and JWS Cook. Quantifying fusion born ion populations in magnetically confined plasmas using ion cyclotron emission. *Physical Review Letters*, 118(10):105001, 2017.

[67] KG McClements and RO Dendy. Ion cyclotron harmonic wave generation by ring protons in space plasmas. *Journal of Geophysical Research: Space Physics*, 98(A7):11689–11700, 1993.

[68] RO Dendy and KG McClements. Ion cyclotron wave emission at the

quasi-perpendicular bow shock. *Journal of Geophysical Research: Space Physics*, 98(A9):15531–15539, 1993.

[69] EG Harris. Plasma instabilities associated with anisotropic velocity distributions. *Journal of Nuclear Energy. Part C, Plasma Physics, Accelerators, Thermonuclear Research*, 2(1):138, 1961.

[70] Setsuo Ichimaru. *Basic principles of plasma physics: a statistical approach*. CRC Press, 2018.

[71] R. O. Dendy, C.N. Lashmore Davies, K. G. McClements, and G. A. Cottrell. The excitation of obliquely propagating fast Alfvén waves at fusion ion cyclotron harmonics. *Physics of Plasmas*, 1:1918–1928, 1994. doi: 10.1063/1.870647. URL http://dx.doi.org/10.1063/1.870647.

[72] DJ Sigmar and G Joyce. Plasma heating by energetic particles. *Nuclear Fusion*, 11(5):447, 1971.

[73] KM McGuire, H Adler, P Alling, C Ancher, H Anderson, JL Anderson, JW Anderson, V Arunasalam, G Ascione, D Ashcroft, et al. Review of deuterium–tritium results from the Tokamak Fusion Test Reactor. *Physics of Plasmas*, 2(6):2176–2188, 1995.

[74] KG McClements, C Hunt, RO Dendy, and GA Cottrell. Ion cyclotron

emission from JET DT plasmas. *Physical review letters*, 82(10):2099, 1999.

[75] CN Lashmore-Davies and DA Russell. Instability of the ion hybrid wave in the presence of superthermal alpha-particles. *Physics of Plasmas*, 4 (2):369–380, 1997.

[76] Tünde Fülöp and Mietek Lisak. Ion cyclotron emission from fusion products and beam ions in the Tokamak Fusion Test Reactor. *Nuclear Fusion*, 38(5):761, 1998.

[77] VS Belikov and Ya I Kolesnichenko. Edge-localized thermonuclear magnetoacoustic-cyclotron instability in tokamaks. *Fusion Technology*, 25(3):258–265, 1994.

[78] Yan Ping Chen and Shih Tung Tsai. Finite banana width effect on magnetoacoustic cyclotron instability. *Physics of Plasmas*, 2(8):3049–3054, 1995.

[79] DK Bhadra, SC Chiu, and RW Harvey. Magneto-acoustic cyclotron instability due to neutral beam injection. *Nuclear Fusion*, 22(6):763, 1982.

[80] Charles K Birdsall and A Bruce Langdon. *Plasma physics via computer simulation*. CRC press, 2004.

[81] Roger W Hockney and James W Eastwood. *Computer simulation using particles*. CRC Press, 1988.

[82] D Winske and N Omidi. Hybrid codes: Methods and applications. Technical report, Los Alamos National Lab., NM (USA), 1991.

[83] Nathaniel J Fisch. Pushing particles with waves: Current drive and α-channeling. *Plasma and Fusion Research*, 11:2101010–2101010, 2016.

[84] Shuhei Sumida, Kouji Shinohara, Ryuya Ikezoe, Makoto Ichimura, Mizuki Sakamoto, Mafumi Hirata, and Shunsuke Ide. Comparison of dispersion model of magneto-acoustic cyclotron instability with experimental observation of 3he ion cyclotron emission on JT-60U. *Journal of the Physical Society of Japan*, 86(12):124501, 2017.

[85] S Sumida, K Shinohara, R Ikezoe, M Ichimura, M Sakamoto, M Hirata, and S Ide. Study on ion cyclotron emissision excited by DD fusion produced ions on JT-60U. 45th EPS Conference on Plasma Physics, 2018. URL ocs.ciemat.es/EPS2018PAP/pdf/P2.1001.pdf.

[86] A Bustos, F Castejón, M Osakabe, LA Fernández, V Martin-Mayor, J Guasp, and JM Fontdecaba. Kinetic simulations of fast ions in stellarators. *Nuclear Fusion*, 51(8):083040, 2011.

[87] Sadayoshi Murakami, Noriyoshi Nakajima, and Masao Okamoto. Finite

β effects on the ICRF and NBI heating in the Large Helical Device. *Fusion Technology*, 27(3T):256–259, 1995.

[88] Masaki Osakabe, Sadayoshi Murakami, Mikirou Yoshinuma, Katsumi Ida, Allan Whiteford, Motoshi Goto, Daiji Kato, Takako Kato, Kenichi Nagaoka, Tokihiko Tokuzawa, et al. Fast ion charge exchange spectroscopy measurement using a radially injected neutral beam on the Large Helical Device. *Review of Scientific Instruments*, 79(10):10E519, 2008.

[89] Masaki Osakabe, Sadayoshi Murakami, Takafumi Itoh, Mitsutaka Isobe, Shinji Kobayashi, Tokihiko Tokuzawa, Kenichi Nagaoka, Haruhisa Nakano, Katsuyoshi Tsumori, Katsunori Ikeda, et al. Evaluation of fast-ion confinement using a radially injected neutral beam in the LHD. *Plasma and Fusion Research*, 5:S2042–S2042, 2010.

[90] F Castejón, LA Fernández, J Guasp, V Martin-Mayor, A Tarancón, and JL Velasco. Ion kinetic transport in the presence of collisions and electric field in TJ-II ECRH plasmas. *Plasma Physics and Controlled Fusion*, 49(6):753, 2007.

[91] P. W. Gingell, S. C. Chapman, R. O. Dendy, and C. S. Brady. Transport and evolution of ion gyro-scale plasma blobs in perpendicular magnetic fields. *Plasma Physics and Controlled Fusion*, 54(6):065005, 2012.

[92] Winske, Dan, Yin, Lin, Omidi, Nick, Karimabadi, Homa, Quest, and Kevin. Hybrid simulation codes: Past, present and future A tutorial. pages 136–165, 2003.

[93] RE Lee, SC Chapman, and RO Dendy. Numerical simulations of local shock reformation and ion acceleration in supernova remnants. *The Astrophysical Journal*, 604(1):187, 2004.

[94] RD Sydora. Low-noise electromagnetic and relativistic particle-in-cell plasma simulation models. *Journal of Computational and Applied Mathematics*, 109(1):243–259, 1999.

[95] Jörg Büchner, Christian Dum, and Manfred Scholer. *Space plasma simulation*, volume 615. Springer Science & Business Media, 2003.

[96] Julius S Bendat and Allan G Piersol. Random data analysis and measurement procedures, 2000.